STUDY OF ONLINE ELECTRON ELASTIC SCATTERING SYSTEM FOR RADIOACTIVE BEAM

By

Ambar C. Rodriguez Alicea

A THESIS

Submitted to
Michigan State University
in partial fulfillment of the requirements
for the degree of

Physics—Master of Science

2024

ABSTRACT

The Facility for Rare Isotope Beams (FRIB) started operation on May 10, 2022, becoming the most powerful facility to study rare isotopes for nuclear astrophysics research. Several facilities in Japan (SCRIT at RIKEN) and in Europe (ELISE at FAIR, GANIL, and DERICA in Dubna) are either in the process of or have already coupled electron linacs to ion storage rings for the possibility to extend scattering experiments from stable to exotic nuclei. Of particular interest is the experimental measurement of the absolute nuclear charge radius for radioactive isotopes, since such information is very scarce and completely unknown for nuclei beyond Bi. Information about the absolute charge radius is a critical ingredient for theoretical models of the atomic structure and parity relations. We investigate the structure for an electron beam that could be coupled to a beamline at the FRIB and perform such scattering experiments. For this purpose, we investigated an electron accelerator facility at Brookhaven National Laboratory (BNL). We also studied new Radio Frequency (RF) acceleration cavities that could be coupled to their system in order to achieve greater energies, as needed for the experiment. We also looked at the trapping potential that such system could achieve, and estimated the achievable luminosity of the system. With these studies, we begin the process to start commissioning a new electron acceleration system that can enhance the scientific reach of FRIB and expand our knowledge of the nuclear structure.

This thesis is dedicated to my daughter, my mother and my beloved shrimp; thank you for supporting me with love and always believing in me. Los amo.

TABLE OF CONTENTS

LIST OF TABLES

LIST OF FIGURES

LIST OF ABBREVIATIONS

SCRIT Self-Confining Radioactive Ion Target 34

SLAC Stanford Linear Accelerator Center 44

SW Standing Wave 30

TW Traveling Wave 30

UV Ultra Violet 24

CHAPTER 1

MOTIVATION

The study of nuclear physics sheds light into the fundamental forces and particles that constitute our universe. The recently upgraded FRIB at Michigan State University represents a significant leap forward in this field. One of the areas where this facility has already contributed, and can continue to do even more, is nuclear structure. Particularly, the absolute charge radii of the nuclei is one of the most fundamental properties of these systems. This measurement is crucial for developing accurate theoretical models of atomic structure and understanding parity relations. Despite its importance, data on nuclear charge radii for isotopes outside the valley of stability is exceedingly scarce, with the most significant contributions dating back to the 1980's.[1],[2] This gap in knowledge hampers the advancement of nuclear theory and its applications. Yet, it remains wildly unexplored In Figure 1.1, we present a compilation of all the existing isotopes, identified by their atomic number Z and number of neutrons N, and highlight those atoms for which the charge radii has been measured. It is important to make the distinction between radius measured using elastic scattering experiments, versus those measured using laser spectroscopy. The later technique, although more precise, can only measure the difference between two isotopes and thus rely on reference atoms measured using other techniques. The only method to this day that can measure the absolute charge radius is elastic scattering. Notice the significant gaps in data even within the stable isotopes starting around Z = 35. This lack of precise measurement leads to uncertainty on other laser spectroscopy measurements as well, as these need to rely on theoretical models to extrapolate for reference atoms.

By coupling an electron linac to the ion beamline at FRIB, researchers can extend scattering experiments from stable nuclei to exotic, radioactive ones. Facilities in Japan, Europe, and now the United States are at the forefront of this innovative approach. This thesis investigates the potential for integrating an electron beam with the beamline at FRIB to perform such scattering experiments. The research presented here focuses on the structure and feasibility of an electron acceleration system that could be coupled with FRIB's capabilities. Detailed studies were conducted at BNL

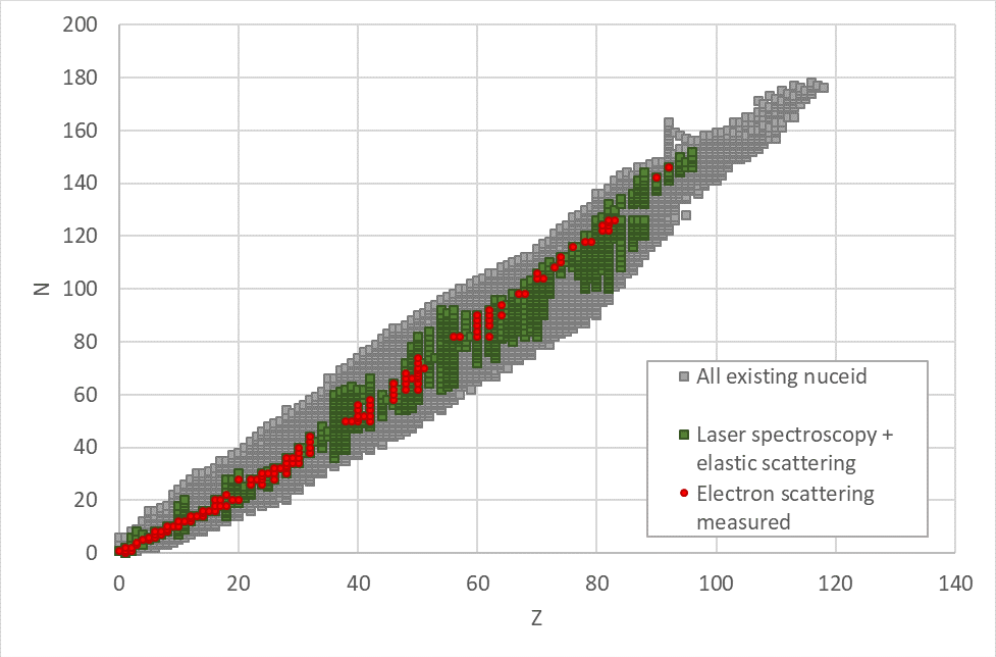

Figure 1.1 Visual representation of all discovered isotopes and those for whose radii has been measured, either using laser spectroscopy or electron elastic scattering.

to explore the design and implementation of new RF acceleration cavities required to achieve the desired energy levels for the experiments. Additionally, the potential for ion trapping and the achievable luminosity of the system were analyzed.

CHAPTER 2

THEORY

2.1 Electron elastic scattering

In the intricate world of nuclear and particle physics, the study of electron interactions has remain a central component for unraveling the mysteries of matter at its most fundamental level. Electron scattering, a phenomenon where electrons deviate from their path due to the influence of forces from other particles, is particularly crucial for understanding the underlying structures and properties of atoms. Among various types, electron elastic scattering, where the electron retains their energy post-interaction, provides insights into the atomic structure. In this section, we will explore the mechanisms of electron elastic scattering, specifically its theoretical foundations.

In a scattering experiment, the object of study is referred to as the target, and it is probed by an accelerated beam of particles with well defined properties. In Figure 2.1 we show the different types of scatterings, where "a" is the incoming probe particle and "b" is the target particle. These interactions are broadly classified into elastic or inelastic processes, with the primary distinction between the two lying in the conservation of kinetic energy.

- Elastic scattering is a process wherein the total kinetic energy of the particles involved is conserved. In this type of scattering, particles collide and deviate from their path, but their total kinetic energy before and after the collision remains unchanged.

- In contrast, inelastic scattering involves a change in the kinetic energy of the particles involved. In these interactions, part of the kinetic energy is transformed into another form of energy, such as heat, mass or light, resulting in a loss of kinetic energy in the system.

- Also depicted in Figure 2.1 are colliding beam reactions. This reaction type could also be elastic or inelastic, but it involves a special type of configuration where both the target and the probing particles are accelerated.[3]

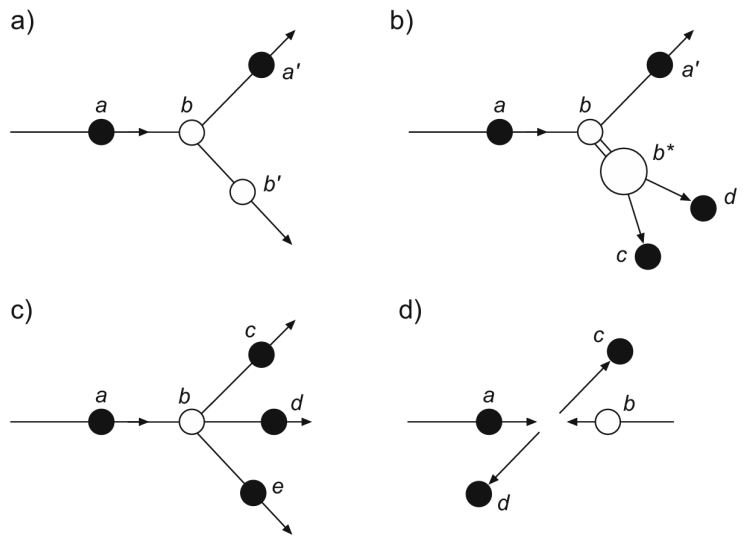

Figure 2.1 Scattering processes: (a) elastic scattering; (b) inelastic scattering– production of an excited state which then decays into two particles; (c) inelastic production of new particles; (d) reaction of colliding beams.[3]

2.1.1 Elastic scattering and nuclear charge radii

For the remainder of our discussion, we will focus on the traditional set up from Figure 2.2, with a fixed target and an incoming probing electron beam. We want to use electrons because its wavelength, when accelerated to a momentum of $p \geq 100$ MeV/c, corresponds to roughly the size of nuclei, $\lambda \leq 10$ fm. Our study spans the energy window of $100 \leq p \leq 1000$ MeV/c.[4]

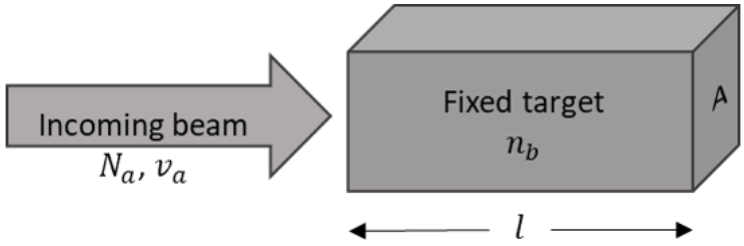

Figure 2.2 Illustration of the scattering arrangement.

The target for scattering experiments may be solid, gas or liquid. In any case, we assume that the molecules or atoms that make up the target have a constant density of n_b, distributed in a volume characterized by a length l and an area A, along and perpendicular to the beam's motion, respectively. The incoming beam interacts with the target via a potential $V(r)$. For very light nuclei, it can be assumed that the nucleus is a "hard circular disk", and thus the first minimum

(θ_{min}) of the angular distribution of the scattered intensity can be used for a rough estimate of the target particle's radius R, as described by equation 2.1.[4]

$$\theta_{min} = \sin^{-1}\left(\frac{1.22\lambda}{R}\right) \tag{2.1}$$

For heavier nuclei, multiple minima are observed. We can describe the interaction using a phase shift analysis using the incoming electron wave function

$$e^{i\mathbf{k}_i\cdot\mathbf{r}}, \tag{2.2}$$

and scattered electron wave function

$$e^{i\mathbf{k}_f\cdot\mathbf{r}}; \tag{2.3}$$

where $\mathbf{p}_j = \hbar\mathbf{k}_j$ is the momentum for $j = \{i, f\}$. The interaction with the nuclear potential $V(r)$ changes the initial wave function 2.2 into the scattered wave function 2.3 with a transition probability given by the square of the charge form factor $F(\mathbf{q})$ that is expressed as

$$F(\mathbf{q}) = \int e^{i\mathbf{q}\cdot\mathbf{r}}V(r)dv \tag{2.4}$$

In this last equation, $\mathbf{q} = \mathbf{k}_i - \mathbf{k}_f$ is the momentum change of the electron (or momentum transferred to the nucleus). In elastic scattering we assume $p_i = p_f$, such that there's only a change in direction described as

$$q = \frac{2p}{\hbar}\sin\left(\frac{\theta}{2}\right) \tag{2.5}$$

Given a potential of the type in equation 2.6, where **r'** is the location of the charges, **r** is the probing location, one can obtain the charge distribution $\rho_e(\mathbf{r'})$ by measuring the scattering probability as a function of the scattreing angle θ.[4]

$$V(r) = -\frac{Ze^2}{4\pi\epsilon_0}\int \frac{\rho_e(\mathbf{r'})d^3r'}{|\mathbf{r} - \mathbf{r'}|} \tag{2.6}$$

For spherical nuclei, the charge distribution depends only on r', and not on θ' nor ϕ'. Thus, we can rewrite the form factor (equation 2.7) as the Fourier transformation of the charge distribution as [4]

$$F(q) = \frac{4\pi}{q} \int \sin(qr')\rho_e(r')r'dr' \tag{2.7}$$

Another relevant observable is the skin thickness parameter t that is typically defined as the distance over which the charge density distribution falls to about 10% of the maximum value (approximately 2.3 fm). When atoms become heavier, they can sometimes deviate significantly from the sphere model: the quadrupole moment can be used to determine the amount of deformation from spherical symmetry.[4]

2.1.2 The Born approximation and higher order corrections

In the Born approximation, the probability for an electron to scatter off a point charge is given by the Mott scattering formula [5]

$$\left(\frac{d\sigma}{d\Omega}\right)_{Mott} = \frac{4Z^2e^4e^2}{q^4c^4}\left(1 - \frac{q^2c^2}{4E^2}\right) \tag{2.8}$$

For energies higher than 100 MeV, we can neglect the electron mass and the Mott scattering formula can be expressed as

$$\left(\frac{d\sigma}{d\Omega}\right)_{Mott} = \frac{Z^2e^4}{4E^2}\frac{\cos^2(\theta/2)}{\sin^4(\theta/2)} \tag{2.9}$$

The condition for validity of the Born approximation is given by the $Z\alpha \ll 1$, where $\alpha \simeq 1/137$ is the fine structure constant.

The Born approximation must be corrected for radiative effects, straggling and dispersive effects that occur during the scattering interaction process. The former accounts for the emission of real and virtual photons, while the latter accounts for only virtual photons. Note that the photons emitted through radiation or straggling must be of very low energies, or else the event wouldn't be accounted as an elastic event (they will be out of the detector acceptance).

2.1.2.1 Radiative corrections

Equations 2.10-2.13 describe the radiative corrections to the Mott cross section.

$$\left(\frac{d\sigma}{d\Omega}\right)_{Mott}^{corr} = \left(\frac{d\sigma}{d\Omega}\right)_{Mott}^{uncorr} e^{-\delta_1(1-\delta_2)} \tag{2.10}$$

$$\delta_1 = \frac{2\alpha}{\pi}\left(\ln\frac{q^2}{m^2c^2} - 1\right)\ln\frac{\Delta E}{E} \tag{2.11}$$

$$\delta_2 = -\frac{2\alpha}{\pi}\frac{13}{12}\left(\ln\frac{q^2}{m^2c^2} - 1\right) + \frac{17}{36} + \frac{\pi^2}{12} - \frac{L_2\cos^2(\theta/2)}{2} \tag{2.12}$$

$$L_2(x) = -\int_0^x \frac{\ln(1-t)}{t}dt \tag{2.13}$$

2.1.2.2 Straggling correction

This effect accounts for the possibility that the electron undergoes multiple small-angle scatterings within the target nucleus. Equation 2.14 describes this correction, where the parameter b is dependent on the atomic number Z and thickness t of the target.

$$\delta_{straggling} = 1 - bt\ln\frac{E}{\Delta E} \tag{2.14}$$

2.1.2.3 Dispersive corrections

This correction accounts for the reduction of the multi-body problem between the incoming electron with the nucleus into the simplified one-body problem of an electron interacting with a static field. It involves an expansion of the Hamiltonian of the system, and will not be further discussed here.[5]

2.2 Beam dynamics

Particle accelerator systems use the electromagnetic force to accelerate, focus and guide the beams. The force felt by electrically charged particles when moving through a magnetic field **B**, and an electric field **E** , with a velocity **v** and charge q, is called the Lorentz Force (equation 2.15). The energy gain of the particle as it crosses the volume with the fields is obtained from equation 2.16.

Although the magnetic field does not contribute in the acceleration of the particle, it plays a vital role in focusing, steering and bendingparticles.

$$\mathbf{F} = q(\mathbf{v} \times \mathbf{B} + \mathbf{E}) \tag{2.15}$$

$$\Delta E = \int_{\mathbf{r_1}}^{\mathbf{r_2}} \mathbf{F} \cdot d\mathbf{r} = q \int_{\mathbf{r_1}}^{\mathbf{r_2}} \mathbf{E} \cdot d\mathbf{r} \tag{2.16}$$

2.2.1 Electron beam emission

The two main processes in which one can generate an electron beam are photoemission and thermal emission. In the photoemission process, powerful laser sources are shone onto a cathode surface, exciting the electrons in the material with sufficient energy to leave the surface as an applied electric field guides them to an accelerating cavity. For the thermal emission, the source of energy for the electrons comes from heating the cathode.

2.2.1.1 Photo-cathode guns

When an electron absorbs a photon, it can be excited from the bound state all the way to a free state in vacuum. This one-step model is very crude and impractical: it assumes that the electron's energy as well as its momentum are conserved. More widely known is the three-step model, which breaks the emission process into: photon absorption and material excitation, transport of the ejected electrons to material surface, and escape into vacuum.[6]

For the first step, we assume that all the energy levels below the Fermi energy (E_F) are filled, while all the energy states above it are empty: this approach idealizes the photocathode material as a conductor at 0 K. One also assumes that the excitation probability is exclusively dependent on the photon energy, and the number of available states for electrons to move from and to (e.g., number of states below and above E_F). From the reflectivity $R(\nu)$ of the material, the probability of absorption $A(\nu)$ into the material, as a function of the incident light's frequency ν, can be calculated following equation 2.17. One would need to also know the material's absorption coefficient at $\hbar\nu$ to determine the absorption depth. As for the number of available states, the probability of exciting the electron

from an energy state E_0 to $E_0 + \hbar\nu$ is given by equation 2.18. In this equation, since we assumed that the momentum is not conserved, the probability of transition is exclusively dependent on the material's electronic density of states. $N(E)$ are the number of states for the energy $E = E_0 + \hbar\nu$, while the integral accounts for the total number of possible transitions.

$$A(\nu) = 1 - R(\nu) \tag{2.17}$$

$$P(E, \hbar\nu) = \frac{N(E)N(E - \hbar\nu)}{\int_{E_F}^{E_F+\hbar\nu} N(E')N(E' - \hbar\nu)dE'} \tag{2.18}$$

After we account for the probability of excitation, we need to consider the probability of the electron to effectively reaches the surface of the material. This process is significantly different for metallic and semiconductor materials. For metallic cathodes, electron-electron (e-e) scatterings are the primordial energy loss processes that inhibit the electron from reaching the surface. On the other hand, e-e scattering are forbidden in semiconductors when the photon's energy is less than double the band gap energy (as is the case for most applications). Thus, electron-phonon (e-p) scatterings is the mechanism that dominates. It is important to mention that one single e-e scattering can reduce the energy of the involved electrons sufficiently for these to be lost, while e-p scatterings mostly affect the electron's momentum, such that an electron can undergo multiple events and still retain sufficient energy to escape.

For metals, we can assume that the probability $S(E)$ of an excited electron with energy $E > E_F$ to interact with another electron of energy $E < E_F$ is purely proportional to the number of electrons with energy E_0, $N(E_0)$, and the number of empty states $N(E_0 + \Delta E)$ and $N(E - \Delta E)$. $S(E)$ is then defined as in equation 2.19, and we can obtain the scattering length $\gamma_e(E)$ from equation 2.20, where γ_0 is an empirical constant of proportionality. Then, the probability that an electron created a distance d from the surface will reach the surface is given by equation 2.21. From this probability, and knowing that the absorption length γ_{ph} is determined by the imaginary part of the index of refraction $n = \eta + ik$ and the incident photon's wavelength γ as in equation 2.22, we can integrate

over all the possible depths of absorption d and get the fraction of electrons reaching the surface without scattering from equation 2.23.

$$S(E) \propto \int_{2E_F-E}^{E_F} \int_{E_F-E_0}^{E-E_F} N(E_0)N(E-\Delta E)N(E_0+\Delta E)d(\Delta E) \tag{2.19}$$

$$\lambda_e(E) = \frac{\lambda_0\sqrt{E-E_f}}{\int_{2E_F-E}^{E_F} \int_{E_F-E_0}^{E-E_F} N(E_0)N(E-\Delta E)N(E_0+\Delta E)d(\Delta E)} \tag{2.20}$$

$$P = e^{-\frac{d}{\gamma_e}} \tag{2.21}$$

$$\gamma_{ph} = \frac{\gamma}{4\pi k} \tag{2.22}$$

$$T(E,\nu) = \frac{\lambda_e(E)/\lambda_{ph}(\nu)}{1+(\lambda_e(E)/\lambda_{ph}(\nu))} \tag{2.23}$$

The multiple scattering events that can happen in the case of a semiconductor make the derivation of an analytical expression practically impossible. For this reason, computational methods, such as the Monte Carlo, are commonly employed to simulate the movement of electrons towards the surface in semiconductors.

The final step, escape into vacuum, requires the perpendicular component of the excited electron's momentum, $k_\perp$, to satisfy the inequality 2.24, where E_{esc} is the necessary energy required to overcome the work function. Note that it is not only necessary that the electron's energy surpasses the work function, but it's direction of motion must also be close to perpendicular with the surface.

$$\frac{\hbar^2 k_\perp^2}{2m} \geq E_{esc} \tag{2.24}$$

More details about the three-step model, and modification to this theoretical framework, can be found in [7]. In terms of losses, the first step accounts for the loss due to reflection of the incident light, the second step reflects on the losses due to scattering processes, while the final step accounts for the loss of electrons for which the direction of motion wasn't at the right angle with

the surface. In general, semiconductors yield higher Quantum Efficiency (QE) due to their band gap. This gap doesn't allow electrons to be excited into states that lack sufficient energy to escape, and additionally it prohibits e-e scatterings. As a result, the mean free path of electrons in metals is much smaller than the laser penetration depth, resulting in unproductive absorption that will never leave the material, while for semiconductors the mean free path can even be larger than the laser penetration, thus fundamentally all excited electrons could potentially be extracted.[6]

2.2.1.2 Thermionic guns

Photoemmission is not the only source for electron beams, thermal emission has also proven to be capable of delivering high average current beams with relatively small radial size. This type of emission is described by the Richardson-Laue-Dushman equation 2.25, for a temperature T, where k_B is the Boltzmann constant and q is the elementary charge. In this equation, the parameter ϕ relates to the work function in absence of external electric field, Φ, as equation 2.26, with F and Q for the classical electrostatic force and the image factor, respectively.

$$\boldsymbol{J}_{RLD} = \frac{qm}{2\pi^2\hbar^3}(k_B T)^2 e^{-\phi/(k_B T)} \tag{2.25}$$

$$\phi = \Phi - \sqrt{4QF} \tag{2.26}$$

2.2.2 Beam focusing and bending

The nominal trajectory in accelerator science stands for the path of an ideal particle, perfectly aligned with every instrument in the system. In real life, accelerator systems deal with bunches of particles, not individual ones, and none of these particles perfectly follows the nominal trajectory. To prevent particles from continuously steering away and being lost to the cavity's wall, focusing magnets are strategically placed to correct for angular divergence and place such particles closer to the nominal path. To look more in detail at the physics of the focusing process, we need to define a Cartesian coordinate system $K = (x, y, z)$ whose origin moves with the center of the beam, thus, the nominal trajectory. The beam motion is aligned with the z axis, while the x axis points in the

horizontal direction and y in the vertical direction. In the areas where a magnetic field bends the beam's direction, the coordinate system K must be adjusted for it. We will assume that this bending occurs exclusively in the horizontal direction, thus rotations are limited to the y-axis. Giving a rotation by an angle φ, the axes x and z are transformed into the axes x' and z' as equations 2.27, or in differential form by equations 2.28.

$$\begin{aligned} x' &= x\cos\varphi + z\sin\varphi, \\ z' &= -x\sin\varphi + z\cos\varphi \end{aligned} \tag{2.27}$$

$$\begin{aligned} \frac{dx}{d\varphi} &= s, \\ \frac{ds}{d\varphi} &= x \end{aligned} \tag{2.28}$$

We assume that the beam moves exclusively in the z direction, such that $\boldsymbol{v} = v_z\hat{z}$, while the magnetic field is only in the transverse direction, $\boldsymbol{B} = B_x\hat{x} + B_y\hat{y}$.

[8]

$$\Delta W = qE\cos\phi \tag{2.29}$$

2.2.3 Beam acceleration

There are two main ways one can accelerate a charged particle, the most intuitive and simple approach is by means of a static electric field. The field is produced by a high voltage Direct Current (DC) supply. The beam would travel between two or more electrodes with increasing voltage, and after the beam exits the area with the static field, it usually continues on a field-free drift tube with constant energy until it hits the target. This method imposes a limitation on the particle's energy based upon the maximum achievable voltage. The maximum voltage that can be developed is primarily limited by corona discharge. The electrons and ions near the high voltage electrode are released with sufficient energy to cause an avalanche when they interact with the residual gas, and thus lead to a breakdown. Up to a few MeV are normally achievable. Yet, the technology is still useful for some application that do not require high energy.

For nuclear physics and big particle accelerator facilities, the customary type of acceleration used today is based on alternating electric fields produced from a RF source. Via this method, the particles travel along a cavity with high-frequency alternating voltage of the form in equation 2.30. This cavity have the particles crossing the electric field when this one is increasing in energy, then they drift through a space without electric field while the field switches polarity, such that when the particles enter the next space, the electric field is again in the acceleration direction for them.[8] A visual representation of these systems is shown in Figure 2.3. We will now proceed to consider the idea of drift tubes that act as Faraday cages and shield the particles from the external source, while the field changes its polarity, as illustrated in Figure 2.3 [a].

$$U(t) = U_{max} \sin \omega t \tag{2.30}$$

Let the particles enter the first drift tube with a velocity v_1, and had then enter i drift tubes with the same shielding condition during the field change of polarity, the particles would have increased to the energy in equation 2.31. In this equation, Ψ_0 is the average phase of the RF voltage the particles perceive as they cross the sections with applied field, and the sine component of Ψ_0 is amplified by the maximum achievable voltage U_{max}. The length of the drift tubes must increase in proportion to the energy gain of the particles, E_i, related to its momentum p_i and velocity v by equation 2.32 and 2.33. Note that we are using relativistic notations, where γ is the Lorentz factor ($\gamma = \frac{1}{\sqrt{1-v^2/c^2}}$), and m_0 denotes the resting mass of the particles.

$$E_i = iqU_{max} sin\Psi_0 \tag{2.31}$$

$$E_i = \sqrt{m_0^2 c^4 + p_i^2 c^2} \tag{2.32}$$

$$p_i = \gamma m_0 v \tag{2.33}$$

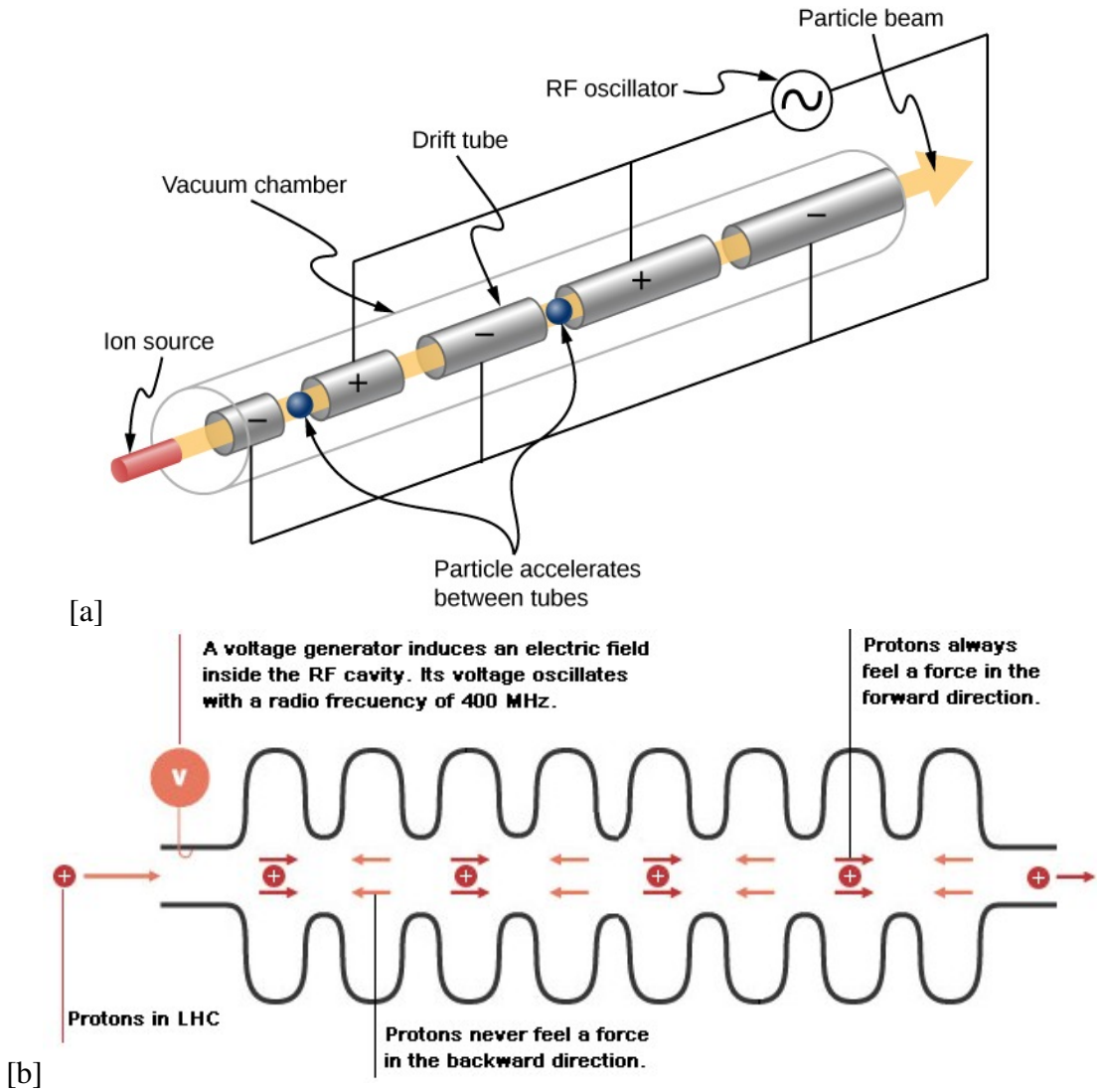

Figure 2.3 Schematics for the basic principles of RF accelerating cavities. [a] Design with alternating polarity drift tubes.[9] [b] Parabolic box cavity design.[10]

$$\gamma = \frac{1}{\sqrt{1-\beta^2}} \quad , \quad \beta = v/c \tag{2.34}$$

We consider the period time τ_{RF} of the electric field, this is, the time it takes the alternating field complete a full cycle as in equation 2.35. Then, the necessary length for a drift tube, such that the particles arrive at the region with electric field when it's back at its peak, must satisfy equation 2.36 for the non-relativistic assumption that $E_i = \frac{mv_i^2}{2}$,[8] and 2.37 for the relativistic energy in equation 2.32. It is noteworthy to mention that because the mass of the electron is so small, its velocity approaches the speed of light with just a few MeV, after which $v \sim c$ and the

length of the tubes remains constant.

$$\tau_{RF} = \frac{\lambda_{RF}}{c} \tag{2.35}$$

$$l_{iNR} = \frac{1}{v_{RF}} \sqrt{\frac{iqU_{max} sin\Psi_0}{2m}} \tag{2.36}$$

$$l_{iR} = \frac{\tau_{RF}}{2} \frac{\sqrt{i(qU_{max} \sin \Psi_0)^2 - im_0^2 c^4}}{\gamma m_0} \tag{2.37}$$

If we have multiple accelerating sections, it would not be unlikely for particles to arrive out of center for U_{max}, and thus becoming out of phase relative to the RF voltage. Ergo, if the cavity is designed for particles to arrive at exactly the maximum power of the voltage, the beam would become unstable and be lost. Instead of using $\Psi_0 = \pi/2$ at the peak voltage U_{max}, some positive degree below Ψ_0 is used at $U_{eff} < U_{max}$. The optimal phase should be around 30°or $\pi/6$, with the exact value dependant on the real structure. A visual concept of this focusing is provided in Figure 2.4. For a structure designed to receive an ideal particle at the nominal phase $\Psi = \pi/6$ at some time t, a slightly faster particle that arrives at the time $t - 1$ would perceive a weaker accelerating voltage than the one at the nominal phase1, $U_{t-1} < U_t$. On the other hand, a particle moving slightly slower and arriving at time $t + 1$, would perceive a voltage $U_{t+1} > U_t$ that would then accelerate it. Thus, this phase promotes a longitudinal self focus. From Figure 2.4, it is clear that a design for maximal voltage amplitude is unstable as it produces the opposite effect; faster particles are still accelerated while slower particles are decelerated as they perceive the field in the opposite direction. Choosing even higher values for the phase, such as $3\pi/2$, cause deceleration of the beam.[8]

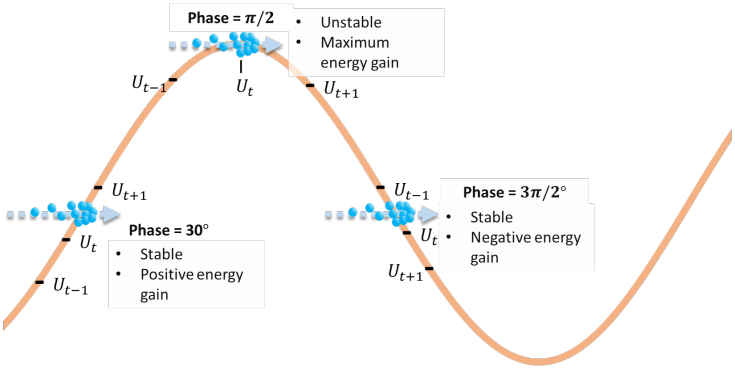

Figure 2.4 Visual representation for the needed phase focusing between the beam and the RF voltage.

CHAPTER 3

TECHNOLOGIES

3.1 Electron Gun

In this sections, we will delve into the intricate details of electron injector systems and their application in high performance environments, with an emphasis in photonic guns. We will briefly discuss the thermal emittance of the beam and how it must be considered in the design, the materials most commonly used in photocathodes, as well as the challenges of operating electron guns. The chapter also presents the latest advancements in photocathode technology, including the design and performance of specific high-efficiency photocathode and thermionic guns. This chapter offers a thorough exploration of electron injectors' complexities, challenges, and the cutting-edge technological solutions developed to optimize their performance.

3.1.1 Beam Emittance, Brightness and Luminosity

An essential aspect of the injector's performance is the beam's emittance and brightness. The brightness of the beam describes its angular divergence, and it is dependant on the beam's emittance, which is the area of the ellipse in the phase space of transverse velocity as a function of position. In concrete terms, the brightness is the ratio of the beam current to the transverse emittance, as shown in equation 3.1.1. This important beam parameter, the emittance ϵ, is determined by the balance between betatron oscillations and damping, which ultimately depends on the magnet structure.[8] Understanding and optimizing both of these parameters is crucial for maximizing the beam's performance.

The space charge effect, the Coulomb repulsion of electrons within the beam bunch, can rapidly increase the emittance, specially so for high current guns. This can be compensated by using extraction voltages above 100 kV. For most high performance applications, somewhere between 400 – 600 kV could suffice. The normalized thermal emittance of the beam, ϵ, when it comes out from the photocathode is directly proportional to the laser spot size σ_{laser}, and to the square root of the electrons' transverse energy kT. Since the beam's brightness is dependant of the emittance,

it is thus dependant on these parameters as well. This can be seen in equations 3.1 and 3.1.1 for the emittance and brightness respectively.

$$\epsilon = \sigma_{laser}\sqrt{\frac{kT}{mc^2}} \tag{3.1}$$

Here, m is the electron's mass and c is the speed of light. The brightness, B_n, on the other hand, is described as

$$B_n = \frac{2I}{\pi^2\epsilon(n,x)\epsilon(n,y)} \tag{3.2}$$

where I is the beam current, and $\epsilon(n,x)$ and $\epsilon(n,y)$ are the normalized emittances in the corresponding transverse planes. More importantly, the maximum transverse brightness for an electron bunch with repetition frequency f, can be described as

$$\frac{B_n}{f} = \frac{mc^2\epsilon E_{cathode}}{2\pi kT} \tag{3.3}$$

where $E_{cathode}$ is the electric field at the cathode surface. Here, it is evident that finding materials with low emitting transverse thermal energy kT, and increasing the electric field at the cathode's surface, is essential for maximizing the obtainable beam brightness.[7]

It is worth noting that the emittance of electron beams have a minimum theoretical value determined by the starting values of the optical functions of the magnets involved the structure. This value must be individually calculated for every system.[8]

Luminosity, in the context of accelerator science, is a term that combines the characteristics of the incident beam and the target to determine the interaction rate per unit cross-section, and has units of $\mathrm{cm}^{-2}\mathrm{s}^{-1}$. This is,

$$L = n_1 n_2 l \tag{3.4}$$

where n_1 is the number of particles per second in the beam, while n_2 is the particle number density of the target and l is the length of the target. Using this, we can define the rate of interactions per

second as

$$\frac{dR}{dt} = \sigma L \tag{3.5}$$

where σ is the cross section for the type of interaction concerned, with units cm^2.[11] We have here assume that the target has homogeneous particle density n_2 and its cross section area is larger than the incoming beam's.

Time averaged luminosity according to [12]:

$$L_{\tau,life}(N_{inj}, \tau_{cycle}) = \frac{1}{\tau_{cycle}} \int_0^{\tau_{cycle}} L_\infty(N_{inj}, \tau_{cycle}) \exp\left(-\frac{t}{\tau_{life}}\right) dt \tag{3.6}$$

where N_{inj} is the number of injected particles, τ_{cycle} is the ion injection period, for isotopes with intrinsic lifetime τ_{life}.

3.1.2 Photoinjectors

For the application at hand, it is said that a source is DC if the duration is longer than 1 μs. This must not be confused with Continuous Wave (CW), which denotes that for each period of an RF cycle a bunch of electrons is present. [7] It is well known that RF accelerating structures can achieve higher acceleration gradients than a DC acceleration structure, resulting in more compact and energy efficient systems. Yet, at the initial stages of beam extraction, DC acceleration offers a simple and stable configuration that can yield lower emittance.[13] Additionally, only DC guns can be used for extraction of spin polarized electron beams, a possible upgrade for the system. For this reason, here I will discuss a hybrid system that uses a high voltage Direct Current to extract the electrons from the cathode, which are then accelerated by one or more RF acceleration cavity.

3.1.2.1 Advanced DC guns

In this section we present two advanced photocathode electron guns. The first gun, an enhanced version of a Jefferson Lab's earlier model, incorporates several upgrades to optimize its performance and reliability. These improvements include a more effective vacuum system, refined motion mechanisms for the photocathode, and a novel approach to cesium deposition for high voltage operations. Additionally, a unique shield door mechanism is introduced to protect the cathode from damage during the high voltage conditioning. The second gun, developed by Cornell, features

a cryogenically cooled design with a Cs_3Sb photocathode. It was constructed primarily from stainless steel and it showcases a unique electrode configuration and a specialized insulator design. The gun's baking and cleaning procedures, must needed to achieve an optimal vacuum environment, are described in details, and the gun's operational characteristics at various temperatures and voltages are also mentioned. Both guns could potentially be used in electron elastic scattering experiments.

Jefferson Lab's high average current gun

The Figure 3.1 depict a newer model of a Cs:GaAs photocathode gun that was made based on the Thomas Jefferson National Laboratory (JLab) 1 kW Demo IR FEL gun [14]. In the newer model, they decreased the vacuum level, added motion mechanisms for better photocathode performance and developed a new method for depositing Cs to allowed a more reliable high voltage operation. One of the new features for photocathode handling included a swing shield door to protect the cathode from back-ion bombardment damage during high voltage conditioning. A detailed schematic inside the ball cathode, that shows the shielding, is presented in Figure 3.2. This gun demonstrated up to 9.1 mA CW beam for a 122 pC bunch with 75 MHz repetition rate.[15]

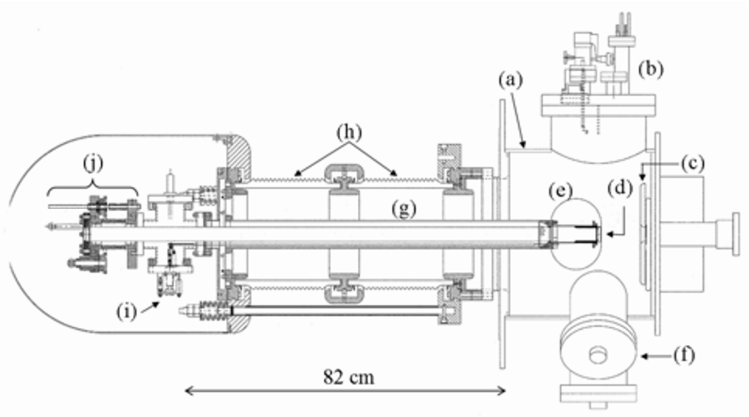

Figure 3.1 DC photocathode gun schematic. (a) vacuum chamber, (b) instrumentation, (c) anode, (d) photocathode, (e) ball cathode, (f) NEG pumps, (g) ball support tube, (h) ceramics, (i) shield door actuator mechanism, and (j) stalk retracting mechanism.[15]

The exposed area of the photocathode has a diameter of 2.54 cm, much greater than the laser spot of 0.8 cm diameter, and it is illuminated off center to reduce QE degradation through back-ion

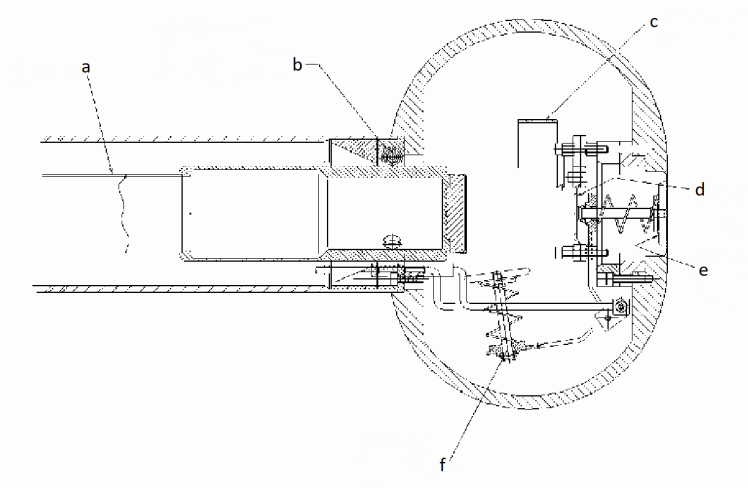

Figure 3.2 Detail of the inside of the ball cathode with the stalk retracted. The shield door is closed only during high voltage conditioning. (a) Stalk retracted, (b) roller guide unit for stalk end - sapphire rollers, (c) charge collector, (d) cesium channels, (e) cathode shield closed, and (f) cathode shield retracted.[15]

bombardment. The cathode is a single crystal GaAs Zn-doped wafer, mounted on a molybdenum disk brazed to one end of the stalk. Before use, the cathode goes through a hydrogen and heat cleaning cycle, followed by baking of the full system, a high voltage conditioning, and finally the photocathode activation to increase QE. The equipment was baked at 500 C for 45 minutes, followed by a longer baking at 250 C until there was no significant vacuum improvement. The electrodes were conditioned to 420 kV, with the stalk retracted and the shield door closed, for about 80 hours to reliably operate at 350 kV. They followed a standard cesium-oxygen activation procedure, as described in [16]. They tested two exact wafers, from the first one a total of 1300 Coulombs were extracted, 100 Coulombs per re-cesiation and 5% QE. With improvements in the vacuum condition and reduction in the beam halo (they installed more pumps and anodized the outermost part of the photocathode), they increased the extracted charge from the second wafer to 500 C per re-cesiation and 7% QE.[15]

Cornell's cryo-cooled gun

Another model for high average current electron gun was recently developed by Cornell. It is a high voltage cryogenically cooled photoemission gun with Cs_3Sb photocathode. The gun walls

were made out of stainless steel, and pure He was used during high voltage conditioning. The system allows for back-illumination of the photocathode, although only standard forward reflecting illumination has been tested. The gun uses two main electrodes, a screening electrode and a spherical shell one. The first one consist of a thin tube that shields against high field emissions at the triple junction of the insulator, High Voltage (HV) stalk and the vacuum, and prevents thermal conduction from the insulator to the cryogenic electrode. The later spherical electrode is made of two joined hemispheres of 316SST vacuum remelt with an internal copper electrode structure, and is where the photocathode is located. The system also has a grounded flat mesh anode, 0.01 cm wire with 22 lines per cm, 2 cm away from the cathode and parallel to the flat surface of the spherical electrode. This grid has two holes, one allows the laser beam to reach the cathode, and the other allow the extracted electrons to fly out. They used an inverted insulator made of AL_2O_3 ceramic with a measured resistance of 16 GΩ.[17] Diagrams and pictures of the system are displayed in figures 3.3 and 3.4.

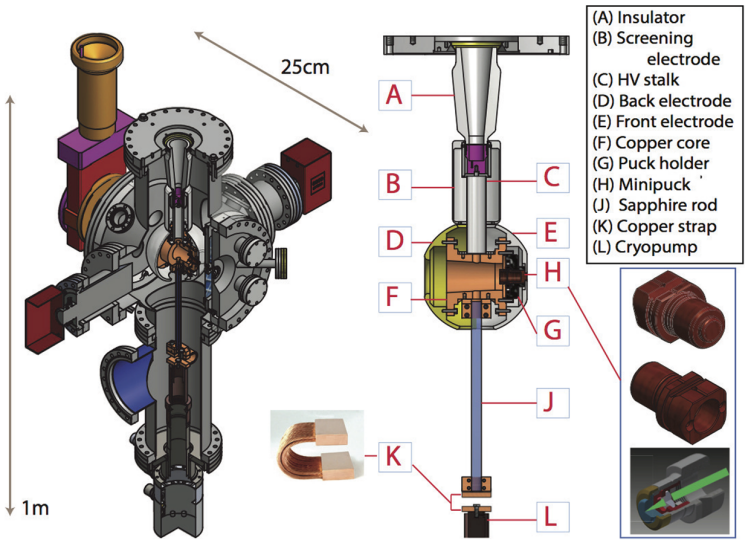

Figure 3.3 Left: A 3D model of the gun. Right: The internal structure of the gun. The two different types of substrate holders (H) are shown. The standard puck (top), is the INFN/DESY/LBNL type used in the FLASHX-FEL gun and on the APEX photoinjector. The modified transmission puck (bottom), was designed and realized to allow the operation of the photocathode in the transmission mode.[17]

To achieve a static vacuum pressure of 2×10^{-11} Torr, they baked chambers and fittings

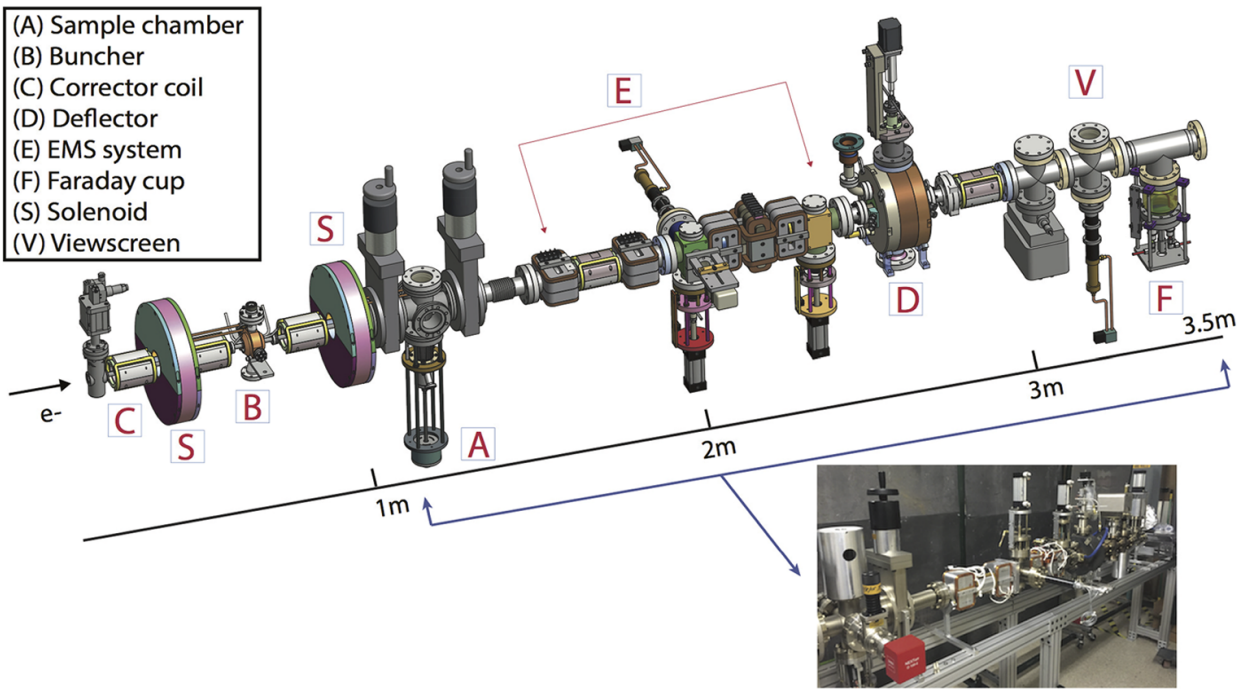

Figure 3.4 3D model of the beamline of the Cornell Cryogenic DC gun.The electron beam enters from the left as indicated by the arrow. The inset shows a picture of the pre-assembled beamline.[17]

individually in air at 400 °C for 5 days, then thoroughly cleaned the components, and carried out a final bakeout, after assembly, at 120 °C for three days. The electrodes were polished with different materials, the finest being diamond suspension of 0.25 μm for the electrode. The HV conditioning was carried out both at room temperature and after the gun was cryogenically cooled down. During room temperature conditioning, highly pure He was introduce into the gun vessel until vacuum was raised above 10^{-5} Torr with ion pumps off, while the voltage of the gun was increased up to $\sim$ 270 kV. The He gas was introduced periodically. Because the introduction of He gas would significantly increase the temperature at the gun, no gas was introduced during the cryogenic conditioning where $\sim$ 300 kV was reached. They set up automatic limits to shut off the HV power supply in order to avoid major voltage breakdowns. The triggers included: four radiation monitors with threshold at 2 mR/h, vacuum level larger than 10^{-8} Torr in the gun vessel, and excess current larger than 300 μA from the supply controller. The temperature for the cathode was 43 ± 1 K in the first sample, and 39 ± 1 K after replacing the photocathode puck with a polished

one. The cooling took 22 to 30 h, with the time required to reach thermal equilibrium steadily increasing.[17]

The cathode is grown and transported under vacuum, avoiding possible contamination from air exposure. It was shine with 500 nm wavelength at 78 MHz repetition rate and 0.5 mW power, to produce 0.1 pC bunches with 10μ A average current and 5% QE. At room temperature, the gun was operated at 230 kV, corresponding to 11.5 MV/m extraction electric fields, and had a beam rms of $\sigma_x = 1.31 \pm 0.07$ mm and $\sigma_y = 1.03 \pm 0.07$ mm. At 43 K, the gun was operated at 190 kV, corresponding to 9.5 MV/m extraction electric fields, and had a beam rms of $\sigma_x = 1.23 \pm 0.07$ mm, $\sigma_y = 1.10 \pm 0.07$ mm.[17]

3.1.2.2 Considerations and Challenges

As of today, semiconductors such as GaAs (the only known cathode that can generate spin polarized electrons), Cs_2Te, GaN, and K_2CsSb, are the most commonly used materials with highest QE and lowest emittance used for photo-production of electron beams. Particularly, QE of up to 20% have been measured for GaAs and K_2CsSb using 520 nm light.[7] High power lasers for this particular wavelength have been commercially available for a long time, with multiple sources offering systems at reasonable prices and high performance.[18],[19][20] The same cannot be said for Cs_2Te and GaN, which require Ultra Violet (UV) light, a spectrum for which no laser system has yet been able to produce enough average power. It is important to notice that even for these materials there is a trade off between QE and thermal emittance.[7] GaAs has demonstrated to be the semiconductor with the lowest thermal emittance.[21] Unfortunately, this minimum happens near it's band gap, as shown in Figure 3.5, where the QE also reaches a minimum lower than 1%.

After deciding the material with which the cathode will be made of, one must caution against the production of "accidental" electrons from scattered light hitting the cathode outside the desired spot. This has become one of the greatest factors limiting the lifetime of cathodes, as these electrons scatter around the chamber producing more electrons, light and ultimately degrading the vacuum conditions. GaAs is one of the most sensible material, requiring vacuum levels under 1×10^{-9} Pa for successful operations. A solution to this problem is to inactivate the outer area of the cathode. This

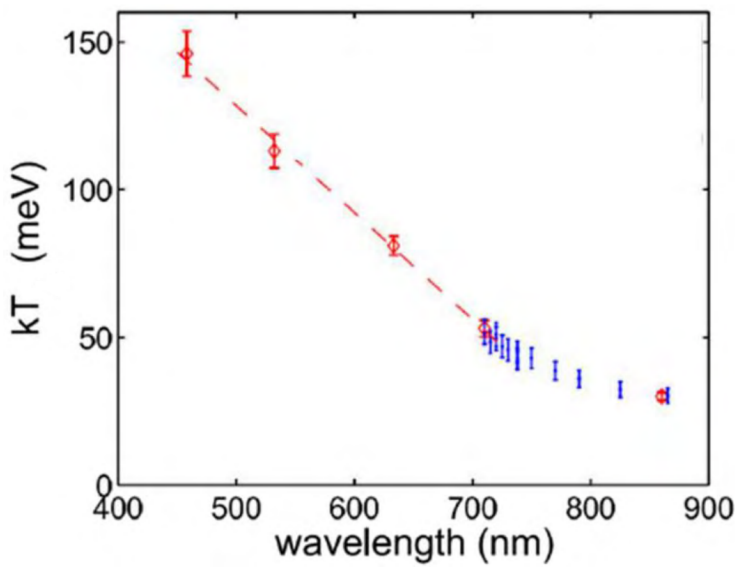

Figure 3.5 Transverse thermal energy for the electrons photoemitted from GaAs as a function of wavelength. The red points were measured using multiple laser spot sizes while the blue points were measured using a single spot size. The dashed line shows a fit over the linear region. kT is the electron's effective transverse energy normal to the cathode's surface.[7]

has been done by coating the cathode with an oxide layer, or masking the surface while activating with cesium.[22] Other mechanisms that limit the lifetime of the cathode are chemical poisoning and ion back-bombardment. These problems can be overcome by the same coating method of the cathode surface. Although this coating could potentially lower the QE, the use of such coating has been demonstrated to deliver higher total currents over the lifetime of the cathode.[23] Improving the vacuum level could significantly extend its lifetime as well.

One of the main sources of vacuum contamination comes directly from the walls of the system, a process known as outgassing. To reduce the hydrogen outgassing, systems are baked at 150 °C for at least 24 hours. The pieces are baked at even higher temperatures and for longer periods of time before assembly. Another way to minimize contamination in the system is to clean each part with high pressure (5×10^5 to 7×10^6 Pa) ultra pure de-ionized water or gas (nitrogen or dry-air) and allowing it to dry in a clean room.[7] A normal spectrum for residual gas found inside a photoinjector system after baking is found in Figure 3.6.

Given the constant high voltages during the operation of electron guns, voltage breakdowns can become a significant problem. In the earlier years of photoemission, Cesium activation (needed

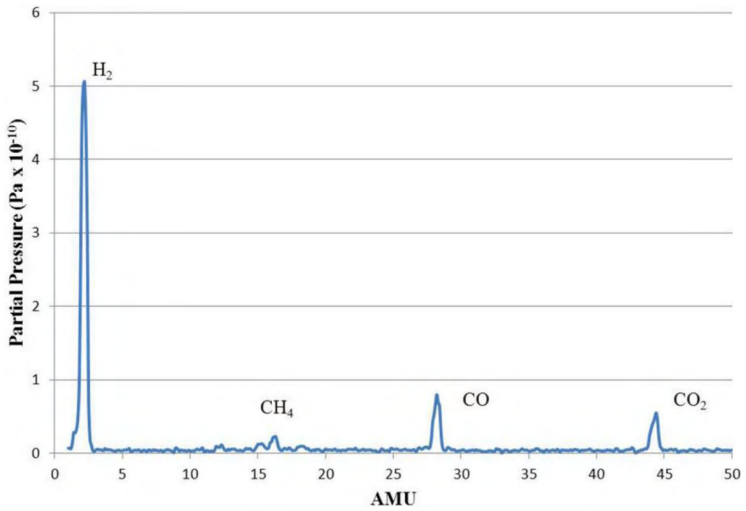

Figure 3.6 Residual gas spectrum after bake-out and non-evaporable getter pump activation, showing hydrogen, methane, carbon monoxide and carbon dioxide. The total pressure measured with an extractor gauge was 6×10^{-10} Pa.[7]

to increase the quantum efficiency) was performed in the same chamber where the experimental extraction was carried on. This contaminant made breakdowns more likely, as it lowers the work function of the electrodes as much as it lowers the cathodes'. Thus, more recent systems include a dedicated-isolated vacuum cavity for the purpose of activation, and from there the cathode is taken into the experimental area by means of a load-lock. Additionally, guns are processed to 10-20% above the operating value, in some cases up to 750 kV maximum voltage, to reduce field emission and arcing.

Another factor that influences the beam's emittance and the behavior of trapped contaminants are stray magnet fields from the system's walls. To minimize these, stainless steel is preferred for vacuum chambers and flanges. Other materials may be used as well, such as molybdenum, copper, or other pure metals. For cathodes and anodes, experiments suggest that the best materials are niobium, stainless steel, or molybdenum for the former, and titanium or beryllium for the later.

It is worth noting that using turbo pumps or cryopumps is advice against, since the vibration caused by these can cause disturbances in the beam during extraction. Instead, ion pumps together with getter pump strips are more suitable for photoemission guns. Every component of the system, buncher, RF cavities, load-lock, or any other, must be maintained under the same vacuum condition

as the gun chamber to avoid contamination.[7]

The development and optimization of photocathodes for electron beam production have made significant strides, particularly with semiconductors like GaAs and alkali antimonides. These materials, offering high quantum efficiency and low emittance, are central to advancing the field of electron injection technology. The balance between quantum efficiency and thermal emittance remains a key area of research, especially in the context of their operational environments and the challenges posed by factors like vacuum contamination and voltage breakdowns. Innovations in cathode design and system maintenance, such as specialized coatings and vacuum techniques, continue to play a critical role in enhancing the performance and longevity of these vital components in electron guns.

3.1.3 Thermionic gun

Another alternative for the electron injection are thermionic guns. These have a simpler design, can be bought from commercial sources at moderate prices, and typically have longer lifetimes than photo-guns. Furthermore, recent advancements in this technology have led to the achievement of remarkably high electron currents, enhancing their applicability in various experimental settings, including elastic scattering experiments.

One notable example of a high current thermionic gun is the LEETCHI system, designed and tested by European Council for Nuclear Research (CERN). LEETCHI is a Pierce-type gun that has the electrode of the cathode holder and the anode electrode at 30°and 45°with respect to the cathode surface. This arrangement prevents beam divergence within the accelerating gap.[24] It uses a commercial cathode assembly that includes a 10 mm planar thermionic emitter and two grids that serve to limit the beam current exiting the cathode. All together, it is capable of delivering a current density of 6 A/cm^2.[25] The gun output current is limited by the cathode temperature and by space-charge effects between the cathode and the first grid. During operation, the extracted beam is accelerated up to 140 keV using DC voltages, then, it is focused and measured by an Optical Transition Radiation (OTR) diagnostic. It is stated that the machine can maintain a constant discharge of 5 A for pulses as long as 150 μs, yet, all the reported optical measurements were

limited to 6 μs pulses to prevent the deterioration of the OTR. When they measured the rms radii of the beam for electron currents of 0.5 A and 5.5 A, they got minimum values of roughly 2.5 mm and 4.1 mm respectively. The emittance was estimated using computer simulations to be between ϵ_{rms} = 35 mm mrad and ϵ_{rms} = 70 mm mrad. All of this was achieved with a vacuum of only 10^{-8} mbar across the full system.[24] A diagram of the beam line can be seen in Figure 3.7, together with measurements and calculations of the rms radii of the collected beam at the OTR.

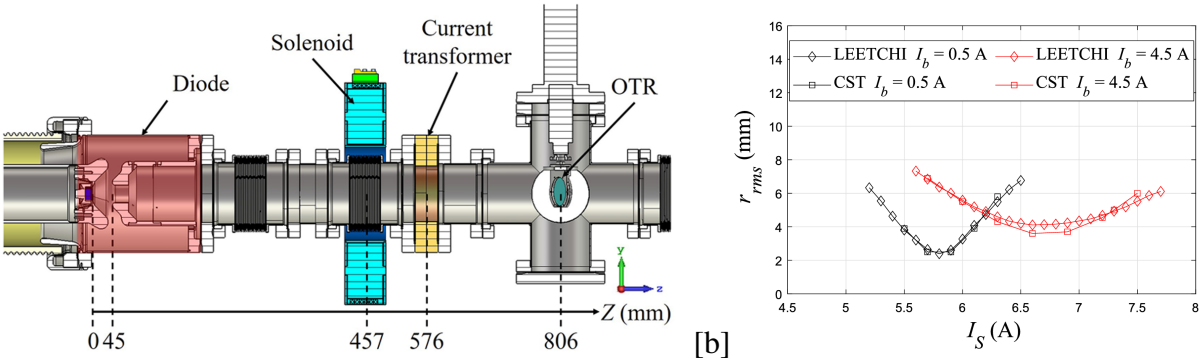

Figure 3.7 [a] Diagram of the layout for the LEETCHI system. [b] Experimental and simulated rms radii for 0.5 A (black) and 4.5 A (red) as a function of the coil current I_s, for a gap between the grid and the anode aperture of 45 mm.[24]

Other systems have been made to deliver up to 100 A/cm^2 current densities over 10,000 hours of operational lifetimes, using advanced cathodes and/or high temperatures at vacuum levels between 10^{-8} to 10^{-7} Torr.[26] Some studies about this using simulations have indicated that guns equipped with LaB_6 filaments can generate a 10 mA average current electron beam with 100 keV energy and normalized emittance of 40 mm mrad, at a filament temperature of 1760 K.[27]

Thermionic electron guns play a pivotal role in various high-current applications, with their design and operational efficiency constantly under improvements. Although this work has mainly focused on the use of photoguns, given the luminosity requirements and the prospect of extracting currents in the order of 1 A using thermionic guns, it is worth taking the time to consider them.

3.2 Acceleration cavities

In this section we will explore electron bunchers, give some general information about RF acceleration cavities, and provide detailed experimental results obtained from an advanced cold

copper acceleration cavity. Each of these components plays a pivotal role in the intricate dance of accelerating electrons to near-light speeds. Electron bunchers, serving as the bridge between initial electron extraction and high-speed acceleration, are instrumental in grouping and preparing electrons for the RF cavities. Their ability to modulate particle velocities and densities is essential for reducing energy spread, thereby ensuring that electrons are suitably prepared for acceleration. This process is critical in maintaining the integrity and efficiency of the entire system. Moving to classical RF cavities, because of the high acceleration gradients needed for rapid energy gain, these structures need to deal with the daunting challenge of managing RF breakdowns, a phenomenon that can cause significant permanent damage. Understanding and mitigating these breakdowns are vital for the longevity and effectiveness of the system. Finally, the development of the Cryo-Cu-SLAC, a high gradient X-band cryogenic copper accelerating cavity, represents a remarkable achievement in this field. Its ability to deliver substantial accelerating gradients while maintaining a manageable breakdown rate is a testament to the ingenuity and collaborative efforts of researchers. Each component discussed in this section – from the precise bunching of electrons to the management of RF breakdowns and the groundbreaking development of the Cryo-Cu-SLAC – represents a critical piece in the complex puzzle of building an electron elastic scattering systems.

3.2.1 Electron buncher

In a typical set-up, electron accelerators consist of a DC gun injector, where electrons are extracted from the cathode, followed by a buncher, that groups the particles into longitudinal bunches and accelerate them into almost the speed of light, and finally, the bunches are accelerated to the desired energies by an RF cavity. It is not uncommon for the buncher to be coupled with the RF elements as one single accelerator assembly. Electrons that come from the gun have uniformly distributed phases and the same energy. Unlike DC acceleration, that is not dependent on phase, once the particles enter the RF cavity, their energy gain is dependent on their phase, as given by the equation 2.29. Reducing the energy spread before entering the accelerating $\beta = 1$ section is the main purpose of grouping the electrons into small phase spread bunches, separated in space by one wavelength in the waveguide.[28]

The simplest bunching technique is known as "ballistic" or "klystron". It uses a stand-alone RF cavity that modulates the particles' velocities, resulting in density modulation after a drift. The cavity is physically separated from the accelerator by a drift space. Another common type of buncher use an accelerating waveguide section with constant phase velocity, which bunches the beam using phase motion. These are known as "tapered bunchers", and are very efficient since they allow for simultaneously accelerate and bunch. They provide the best capture rate and allow for specific beam parameters to be achieved, but because of their complexity, it is the most challenging design.[28]

In a system from Los Alamos National Laboratory, as an example, the initial bunch length after exiting the gun is approximately $30 - 40$ ps, then it is compressed to $5 - 10$ ps using a normal conducting RF buncher cavity, and it is further compressed while passing through several super conducting RF cavities to achieve a bunch length of $1 - 2$ ps. The system also includes several solenoid focusing magnets that control the beam size and emittance.[7]

3.2.2 Classical cavities

RF breakdowns is one of the major limiting factors for higher accelerating gradients. We call an RF breakdown when the transmission and reflection power abruptly and significantly changes while emitting a burst of X-rays and visible light. The specific change of RF power for Standing Wave (SW) and Traveling Wave (TW) are different, but both cause damage to the accelerating structure, as well as the RF components and sources. In the case of TW, the transmitted power drops and up to 80% of the incident power is absorbs. On the other hand, the input RF power is reflected for SW structures.[29] Typically, RF breakdowns are separated into trigger and secondary. While the secondary breakdowns appear to be caused by the damage caused by the trigger breakdown, the trigger breakdown is understood to be dependent on material properties and structure geometry. Some of the things that can affect the rate of breakdowns are pulsed surface heating, peak electric and magnetic fields, peak Poynting vector, hardness of the cavity material, among others. Peak RF pulsed heating is more important for SW, while RF electric peak fields matter most for TW structures.[30]

When measuring the RF breakdown rates, the RF power into the structures is slowly increased. The number of breakdowns is recorded and the official breakdown rate is obtained once the rate stabilizes and remains constant for hours. Variability in the original state of the metal surface, due to different manufacturing methods and surface preparations, make the initial state of breakdowns irreproducible. The breakdown rate nonetheless can be reproduced, and it is dependant on the structure geometry and material, as well as working conditions.[29]

It has been empirically found, with some theoretical models agreeing, that the breakdown rate, BDR, depends on the accelerating gradient. G, as $BDR \propto G^{30}$ for many TW structures.[30]. Numerous studies have been carried out to increase the accelerating gradient while decreasing the RF breakdown rate. One study found that heat-treated structures (those that used brazing or diffusion bonding for manufacturing) result in significantly higher breakdown rates.[31] Other methods like wielding and electroforming (deposit copper onto aluminum mandrel in an electro-chemical bath and subsequently removing the aluminum by etching) have been suggested as alternatives for high gradient accelerating structures.[29]

3.2.3 Cold copper acceleration cavity

SLAC National Accelerator Laboratory, in collaboration with the University of California - Los Angeles and Cornell University, have developed a high gradient X-band cryogenic copper accelerating cavity, Cryo-Cu-SLAC, that has proven to deliver up to 250 MV/m at 45 K with 10^8 RF pulses. Furthermore, this accelerating system reached the highest accelerating gradient for X-band RF structures maintaining the same breakdown rate of other structures with lesser accelerating gradient. It must be noted however that by running the machine at gradients higher than 150 MV/m considerable structural degradation was observed, and therefore a trade-off must be made to preserve its operational lifetime.[30]

Since it is currently understood that breakdowns are caused by movement of crystal defects, induced by periodic mechanical and/or thermal stress, it was theorized that cryogenic temperatures could decrease such mobility and stress, thus decreasing the total RF breakdown rate. This was the primary motivation of the group to develop the Cryo-Cu-SLAC. Reducing the cavity temperature

to below 77 K decreases the RF surface resistance and coefficient of thermal expansion, and it increases the yield strength and thermal conductivity. These changes decrease the pulsed surface heating and mechanical stress experienced by the cavity. The decrease in RF surface resistance has been extensively studied, and in cryogenic copper the phenomena can be described by the theory of anomalous skin effect.[32] Unluckily, there are not many studies of copper cavities at temperatures below 100 K with high input RF power corresponding to fields greater than MV/m. More so, one study showed a decrease of the intrinsic quality factor, Q_0, with increasing fields at 3 GHz, 77 K and surface electric fields of up to 300 MV/m. This study did not reported the observed breakdown rate.[33]

The structure developed by SLAC, Cryo-Cu-SLAC, is made of three cells with the highest field in the middle cell, and it is shaped to mimic the properties of longer periodic structures. It has a small aperture of $a = 2.75$ mm and elliptical shaped irises of 2.0 mm thickness. It was design to be critically coupled at 96 K with $Q_0 = 19,100$, under-coupled at 293 K and over-coupled at 45 K, using a TM_{01} mode launcher as the RF power coupling. This cavity didn't have field probes, as they distort surface fields and degrade high power performance. Instead, they measured the input/forward RF power, reflected RF power, and signals from current monitors that intercept the field emission currents, to determine the electric field in the cavity. Its resonant frequency is 11.424 GHz at 150 K, and 11.4294 GHz at 45 K.[30] Other parameters are shown in Table 3.1.

The cavity was in contact with the head of the pulsed cryocooler Cryomech PT-415, and placed inside a vacuum cryostat. A heat shield of 0.015 in copper foil was placed in between the SW structure and the rest of the cryostat, before the current monitor, to prevent contamination of the accelerating structure from gases of the vacuum of the cryostat. A diagram of the system can be seen in Figure 3.8. The source for the RF power was a SLAC 50 MW XL-4 klystron, with repetition rate of 5, 10, or 30 Hz and pulse length of up to 500 ns.[30]

The studies with Cryo-Cu-SLAC found that lowering temperatures allowed to sustain larger RF surface electric fields with decreased probability for breakdowns. Still, Q_0 decreased with increase in the accelerating gradient due to dark current beam loading. The processing history of the cavity

Parameter	293 K	45 K
Q-Value	8,590	29,000
Shunt impedance [MΩ/m]	102.891	347.39
Hmax [MA/m]	0.736	0.736
Emax [MV/m]	507.8	507.8
Eacc [MV/m]	250	250
HmaxZ0=Eacc	1.093	1.093
Losses in a cell [MW]	7.97	2.36
Peak pulsed heating (150 ns) [K]	86.9	21.9
a [mm]	2.75	2.75
a=λ	0.105	0.105
Iris thickness [mm]	2	2
Iris ellipticity	1.385	1.385

Table 3.1 Parameters of periodic accelerating structure with π phase advance per cell and dimensions of the Cryo-Cu-SLAC middle cell at 45 K and 293 K. Fields are normalized to E_{acc} = 250 MV/m for f_0 = 11.424 GHz. Peak pulsed heating is calculated for a pulse with 150 ns flat gradient.[30]

for high power measurements, recordings of the acceleration gradient and breakdown accumulation as a function of pulses, is presented in Figure 3.9. For the accelerating gradient after 70×10^6 pulses, they measured an RF trigger breakdown rate of 2×10^{-4} /pulse/m and a total breakdown rate of 2×10^{-3} /pulse/m for a shaped pulse with 250 MV/m, corresponding to 507 MV/m peak surface electric field, and 150 ns flat gradient. These rates were measured for periods of 1-3 million pulses where the gradient and rate of trigger breakdowns were relatively constant.[30] We can see how the breakdown rates for the Cryo-Cu-SLAC compares with measurements of other equivalent shape (2.75 mm aperture radius) accelerating structures of different materials at room temperatures is presented in Figure 3.10.

3.3 Ion trap

For the discussion of ion traps, we will focus on the pioneering work conducted at The Institute of Physical and Chemical Research (RIKEN), Japan. We first set the stage by detailing the components of RIKEN's sophisticated electron-ion elastic scattering system, which includes specialized equipment such as a race track microtron, an electron storage ring, and a unique electron-beam driven rare isotope separator, among others. We then dive into a detailed exploration of the SCRIT device, its trapping efficiency, the overall setup and details of the electron beam performance. The

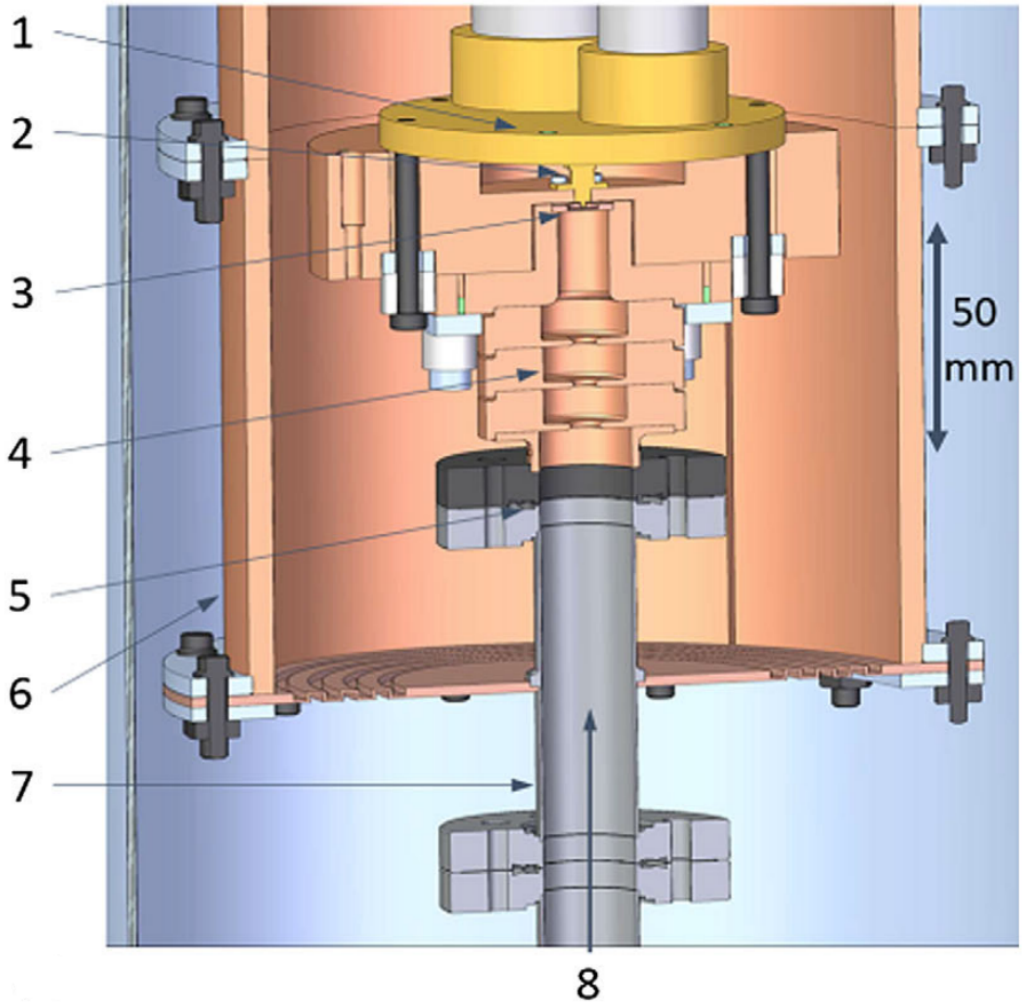

Figure 3.8 Solid model of the cryostat zoomed-in. (1) Cold head of cryocooler; (2) current monitor; (3) brazed metal foil; (4) Cryo-Cu-SLAC; (5) RF flange; (6) thermal shield; (7) Cu-plated stainless steel waveguide; (8) RF input.[30]

facility's capacity to achieve a high luminosity for stable ions was only the beginning of their trajectory to become the first facility to measure short-lived nuclei; isotopes that have been out of the reach for electron scattering for decades. This section not only showcases RIKEN's technological prowess, but also underlines the importance of such advanced systems in pushing the boundaries of nuclear physics research.

The Self-Confining Radioactive Ion Target (SCRIT) system at RIKEN was design to perform precise measurements of the atomic charge radii for short lived radioactive isotopes, and has already demonstrated it's capabilities with the first ever measurement of electron elastic scattering off ^{137}Cs

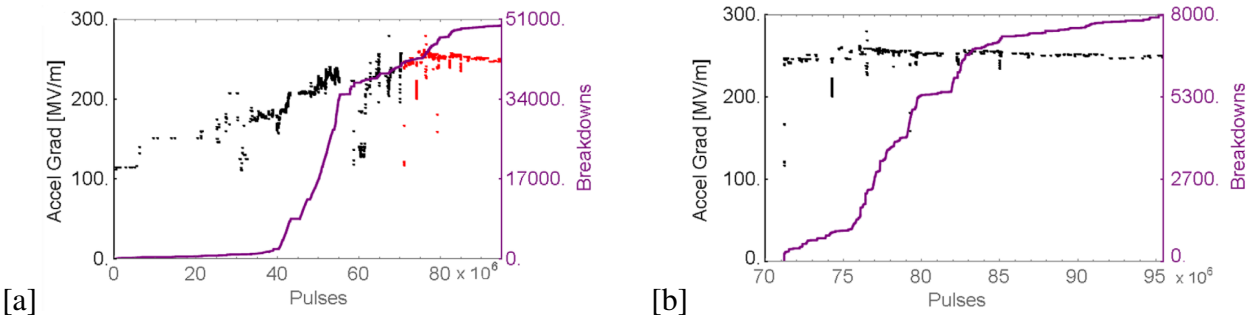

Figure 3.9 The processing history for Cryo-Cu-SLAC. [a] Purple is the number of accumulated breakdowns. Black and red points are the calculated average gradient. Red indicates the time period where breakdown rate was measured. [b] Zoom in of the same data for the period where breakdown rate was measured.[30]

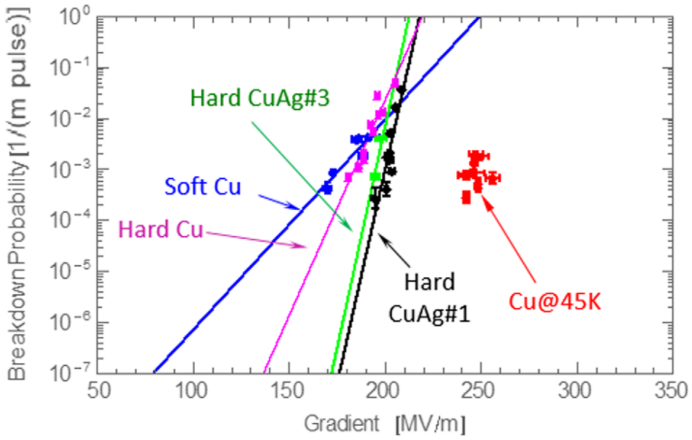

Figure 3.10 Total breakdown rate as a function of accelerating gradient for diferrent structures.[30]

last year. Measurements showed up to 10^{27} $cm^{-2}s^{-1}$ luminosity for stable ions with 250 mA electron beam current, and average luminosity of 0.9^{26} $cm^{-2}s^{-1}$ for unstable isotopes.[34][35] The system design consist of a 150 MeV race track microtron (RTM) for electron beam generation, a repurposed electron storage ring (SR2) donated from the National Institute of Advanced Industrial Science and Technology for electron charge accumulation, an Isotope Separation On-Line (ISOL) system, an electron-beam driven rare isotope separator (ERIS), a DC to RF converter (FRAC), a luminosity monitor (LMon) and a window-frame spectrometer for electron scattering (WiSES). A schematic of the system is presented in Figure 3.11. The storage ring is a second generation synchrotron, composed of a four dipoles and two straight 3.5 m sections for a total circumference of 20 m. These components work in synchrony to generate, accelerate, and accumulate electron

beams, as well as to produce and select rare isotopes for experimentation. The ring takes the 150 MeV injected electron beam and can accelerate it up to 500 MeV.[12]

Central to the SCRIT system's operation is its innovative ion trapping mechanism located inside the electron ring and illustrated in Figure 3.12. This setup allows the system to hold up to 10^8 ions in a 500 mm length.[36]. When the ions are dumped into the SCRIT device, at energies of about 6 keV, they essentially form a three-dimensional gas target. The recirculating electrons provide transverse focusing, while simultaneously serving as probe for elastic scattering, and a mirror potential, described in more details below, provides longitudinal trapping.[12] For an electron beam current of 250 mA, used normally during data collection, the transverse potential depth produced is roughly 50 V.[34] Data is taken for 1 to 2 s, after which the beams are dumped and the accumulation of electrons starts again.

The SCRIT device has one main electrode structure, with dimensions $99(\mathrm{h})\times115(\mathrm{w})\times(\mathrm{d})$ mm^3, and two sub-electrodes. The main composite electrode structure is made of a combination of two 3 mm thick electrodes at the top and bottom, and thin 0.1 mm thick mesh electrodes on both side walls. In order to allow the scattered electrons to enter the detectors, no mesh was placed horizontally over the 35 mm center of the vertical direction. Outside here, the mesh was extended for 8 mm in the horizontal and 5 mm in the vertical direction respectively. The sub-electrodes, used to produce the 6 keV barrier potential, are made of a 2 mm diameter wire in a birdcage-shaped racetrack at both ends of the main electrode.[36] The careful design of these electrodes, including the use of mesh and wire components, facilitates the trapping of ions while allowing scattered electrons to reach the detectors.

During injection, the electron beam power is around 0.4 W at a 2 Hz repetition rate, the repetition rate is later increased for the ion beam production to 20 Hz, which increases the power to 20 W. The peak current for the microtron is almost 3 mA, while at the storage ring 300 mA current is maintain for 1 h lifetime. The cooler buncher system consists of six quadrupole electrodes and a set of einzel-lens and other electrodes for a total length of 950 mm. This buncher converts the continuous ion beam into a 500 μs pulsed beam.[34] The measured electron beam size is about

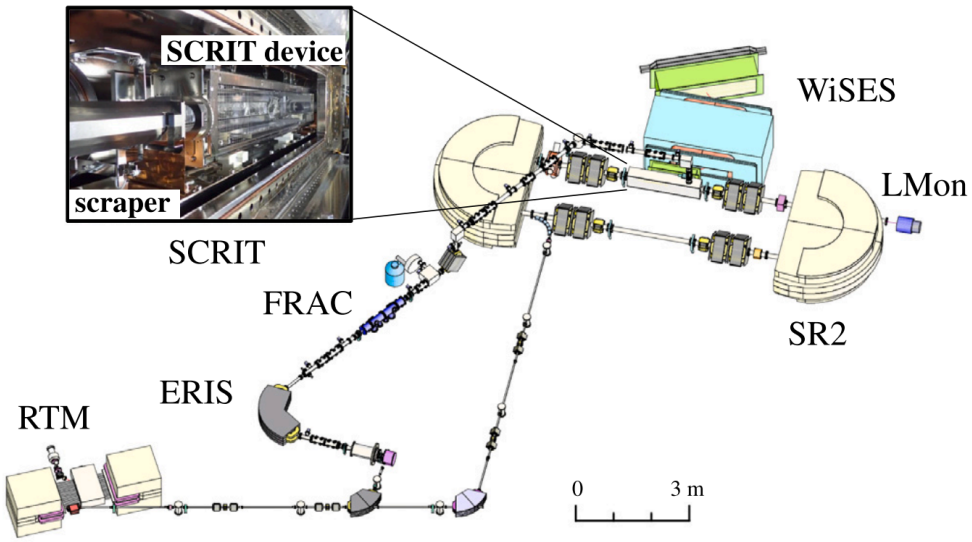

Figure 3.11 Schematic of the SCRIT electron scattering facility. A picture of the SCRIT device in the vacuum chamber is included in the figure.[36]

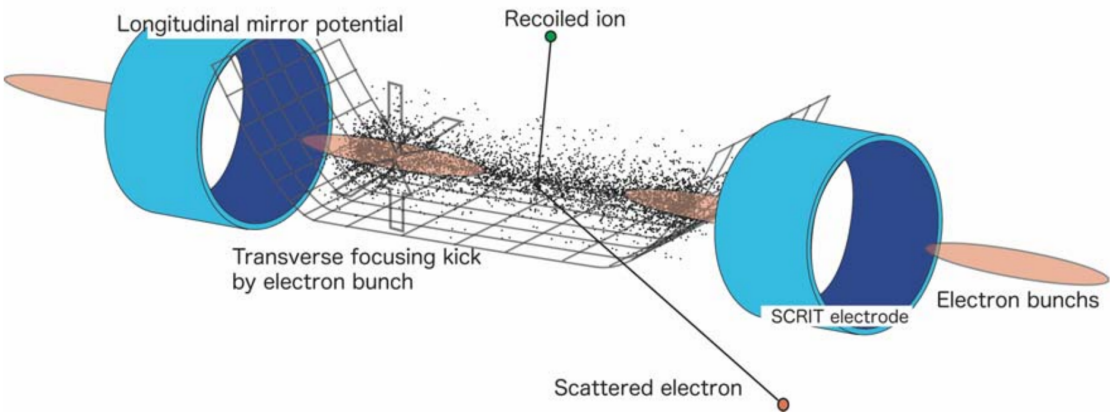

Figure 3.12 Ion trapping concept of SCRIT.[12]

2 mm in the horizontal and 0.4 mm in the vertical direction. Once accumulation is completed, the electron beam is deflected before entering the ring to irradiate a uranium carbide target to produce rare isotopes through photo-fission reactions. The rare isotope beam are selected based on mass and accumulated at FRAC and subsequently dumped at SCRIT where they are trapped and ready for data collection. Investigations of the efficiency of the trapping system have yield a maximum trapping efficiency, as defined in equation 3.7, of ϵ_{trap} = 42%, and a overlap efficiency, defined in equation 3.8, of ϵ_{over} = 42%, for currents between 200 – 230 mA.[36]

$$\epsilon_{trap} = N_{trap}/N_{inj} \tag{3.7}$$

$$\epsilon_{over} = N_{col}/N_{trap} \tag{3.8}$$

In these equation, N_{col} refers to the number of ions colliding with the electron beam, N_{trap} refers to the number of trapped ions, and N_{inj} is the number of injected ions.[36]

In a paper published before the full system was constructed, they proposed to measure the recoiled ion in coincidence to the scattered electrons in order to determine the mass of the ion. This was possible given that the ions are practically static in contrast to the electrons. The momentum transfer from the electron to the ion, q, for an electron energy E_e and electron scattering angle θ, is given by the equation 3.9. Using this and equation 3.10, they can determine the mass m of the ion from the time of flight T.[12]

$$q = 2E_e \sin(\theta/2) \tag{3.9}$$

$$q = Am\frac{L}{T} \tag{3.10}$$

3.4 Detectors

The basic components of a detection system for electron elastic scattering experiments are position sensitive detectors, particle's energy detectors and beam monitors. As an example, the detection scheme for SCRIT is made of a window-frame dipole magnet with one front and one rear drift chamber filled with He+C_2H_6 (80:20) gas and a He gas vinyl bag in between them, two 2 m long plastic scintillators for trigger, and several additional scintillators for background noise canceling. In this scheme, the drift chambers determine the particle's position and angle, and coupled with the dipole magnet, the energy can be calculated as well. The trigger plastic scintillators provide the timing of the ionization events. This system has a solid angle of about $\Omega \sim 80$ msr, and a momentum resolution of $\Delta P/P \sim 3 \times 10^{-3}$ at 300 MeV.[36] As for the beam

monitor equipment, different types of screens are used to measure the beam's profile, and the most common method of measuring the absolute charge of the beam are Faraday cups. Other methods, such as secondary emission monitor and ferrite-core pulse transformer, are also available, and some of these measurement techniques can even be employed together.[37] The first component of WiSES detector system at SCRIT is a window-frame dipole magnet with maximum field of 0.8 T and gyroradius of 1250 mm at momentum p = 300 MeV/c, followed by the hexagonal drift chambers and plastic scintillators. This system covers scattering angles of 30°to 60°. The luminosity monitor measures the bremstrahlung photon produces at the exit of the SCRIT device. More information about the details of these detector system can be found in [34].

Magnetic detector systems must have good resolution, which is influenced by the detector size, it's intrinsic resolution and the beam spot size, and its magnetic field uncertainty must be a small fraction of the resolution width. The detector must also be shielded against background noise, and be usable over a broad range of momentum transfer and scattering angles. The concept of one of the smallest resolution spectrometers is illustrated in Figure 3.13. The idea is that a momentum dispersed beam is spatially focused on a spectrometer target, and if properly matched, all electrons then arrived on the spectrometer focal plane based on their energy loss with the target, regardless of their initial energy.[37] For multi-wire chambers, discussed in details below, what mostly limits their spatial accuracy is the distance between anodes, which has a practical limitation of about 2 mm.[38]

The drift chambers, strategically placed at the front and rear of the dipole magnet in the SCRIT system, are widely used in accelerator science for particle tracking, and they are part of the broader family of wire proportional chambers. Multi-wire proportional chambers, first invented by CERN in 1967, consist of thin parallel and equally spaced grounded wires (anodes) placed symmetrically between two cathode planes. A diagram, together with the electric field of this configuration, is shown in Figure 3.14. The gas gaps are usually two or three times larger than the spacing between the wires. Electrons created in the gas by an ionization event drift along the field lines and, as they approach the anode wires, an avalanche multiplication takes place when strong voltage at the

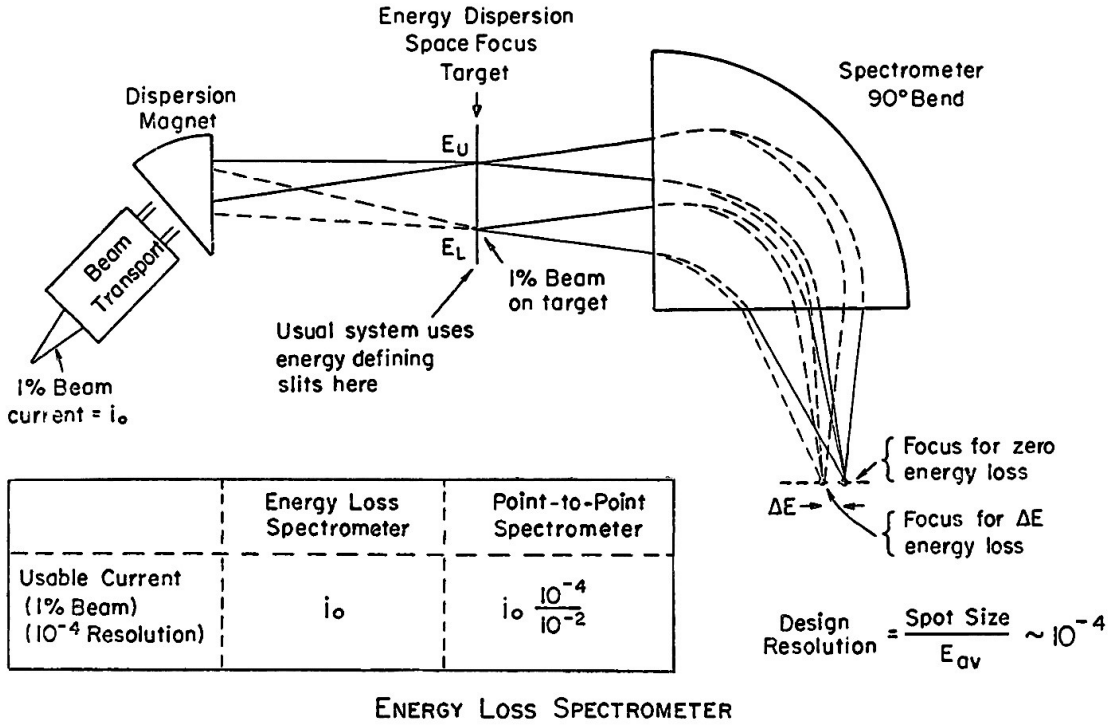

Figure 3.13 Concept of the energy loss spectrometer system developed by MIT.[37]

cathodes are employed.[38]

The simplest design for these is a single wire, in which a single-cell drift chamber has a narrow gap of constant electric field with a wire at one end. The electrons created when energetic particle beams pass through the gas chamber are amplified once they reach the wire and a signal is detected. This method requires a time reference signal of the ionization event, which is mostly provided by scintillator counters in coincidence. The biggest working apparatus of this configuration reached 50 cm drift length, with a voltage around 50 kV and a maximum drift time of about 10 μs. With a single cell, the position resolution rms is limited from about 0.5 to 1.5 mm. In contrast, position accuracy better than 400 μm rms was achieved using a multi-cell planar drift chamber in 1973.[38]

The multi-wire proportional chambers are typically modified to allow for reduction of low field regions in the central plane. One of the first modification had the anode wires alternate with thicker field wires to reinforce the electric field in the critical area and reduce the signal cross-talk between adjacent cells. The main drawback of multi-cell drift structures is the uniform electric field across the active cell, as shown in Figure 3.15, which causes distorted space-time

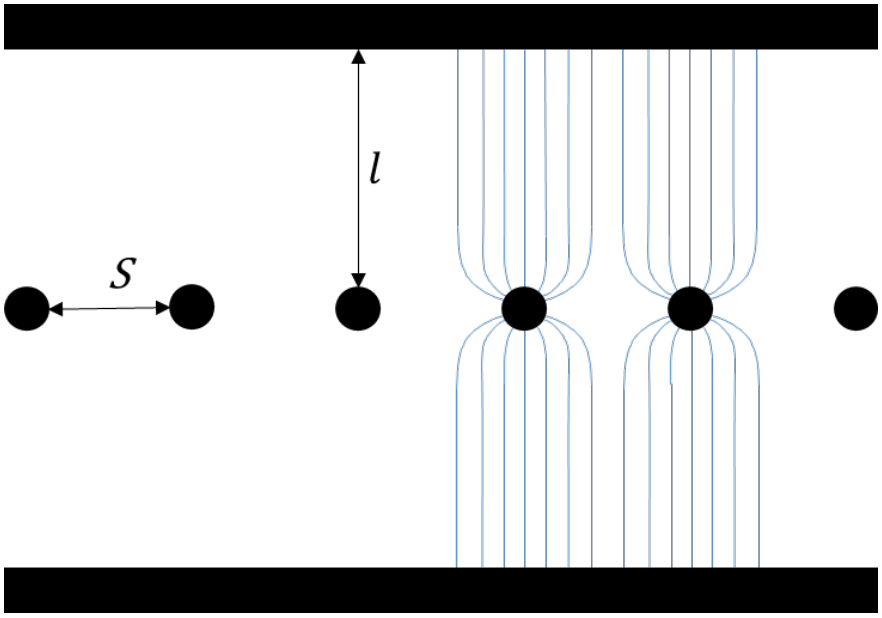

Figure 3.14 Schematic for the concept of multi wire proportional chambers, where l is the distance between the wires and the cathode plane, S is the separation between the anode wires, and the blue lines are the electric field lines.

correlation. Even so, they remain one of the top choices for experiments given their large detection area, short memory time and high spatial accuracy. One way to improve the localization accuracy is by operating the structure at high pressures, which decreases diffusion and increases ionization density. There are also configurations that employ two sets of parallel cathode wire planes centered around the positive anode wire, and are symmetrically connected to increasingly high negative potentials, with additional field wires at the adjacent cathode's potential and grounded screening electrodes that isolate the system. These are so called high accuracy drift chambers, as the field distribution is almost equipotential and uniform, thus resulting in a linear correlation of space and time, almost independent from the incident angle. A simple diagram of such configuration is shown in Figure 3.16. In any case, for an optimal track reconstruction, it is required to calibrate the machine such that the space-time correlation is very well known.[38]

Contrary to the multi-wire chamber, the position resolution of the drift chambers is mostly dependent on the knowledge of the space-time correlation and the intrinsic diffusion properties of the migrating electrons. Due to the symmetry of the system, right-left ambiguity must be solved using reconstruction tracks of measurements from different planes. A measurement of the charge

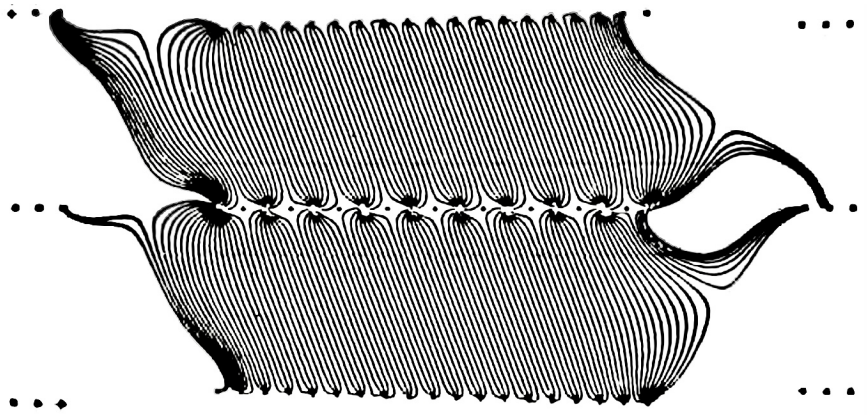

Figure 3.15 Drift lines for electrons in a cylindrical drift chamber with 0.45 T magnetic field parallel to the wires.[38]

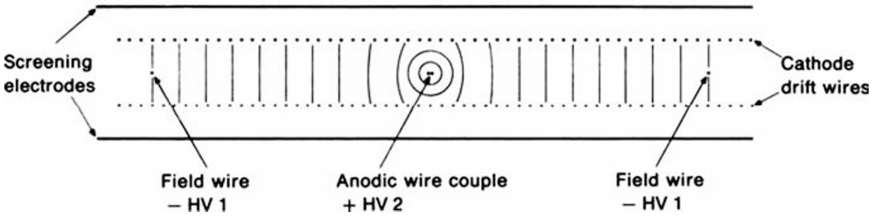

Figure 3.16 Diagram of a high accuracy drift chamber.[38]

shared between the two ends of the wire provides the longitudinal coordinate for the event.[38]

Although any gas or mixture of gasses can produce avalanche multiplication, the selection of a specific filling is made based on the requirement parameters, this is, working voltage, operational gain, proportionality, rate capabilities, lifetime and recovery time. Noble gasses can achieve avalanche multiplication at the lowest voltage field, argon being the preferential gas for monetary and minimum ionizing particle detection reasons. Yet, one most be cautious about the potential of permanent discharge, for which introduction of compound gases, such as hydrocarbons or those in the alcohol family, dissipate the excess energy by the absorption of the photons emitted by argon and avoid entering a permanent regime of discharge. The same effect can be achieved using polyatomic quencher. Argon-ethane or argon-methane are common mixtures used in wire proportional counters. Gains above 10^5 can generally be obtained before breakdown. The time resolution for efficient detection of a typical multi-wire proportional chamber is about 30 ns for a 2 mm separation of wires.[38]

A concept developed at Stanford by H. W. Kendall that allows for precise measurement of the momentum of scattered electrons involves a series of small detectors placed along the focal plane of a spectrometer. The primary purpose of these ladder counters is to detect the position at which each electron intersects the focal plane of the spectrometer. By doing so, each detector in the ladder corresponds to a slightly different momentum bin of scattered electrons for any given magnetic field in the spectrometer. Since the momentum of electrons after scattering depends on the scattering angle and the energy transfer during the interaction with the target, determining their position at the focal plane directly contributes to the analysis of the electron's momentum. Ladder counter systems can made of plastic scintillators, semiconductors or multi-wire spark chambers. Plastic scintillators have the advantage of high count rate probability, given by their fast response and rapid recovery. One case of a semiconductor ladder system was employed by the National Institute of Standards and Technology using lithium-drifted silicon semiconductor detectors. These detectors are compact and easy to stack and shield, but they require cooling for fast collection times in the order of nm, and are highly sensitive to radiation damage and surface contamination, giving them an average of one or two years of useful lifetime. Finally, the spark chambers have similar spatial resolution and size to semiconductors, with the drawback of poor background rejection and counting rate limitations.[37]

CHAPTER 4

ANALYSIS

4.1 Computational modeling

4.1.1 Capabilities and specifications of ATF

The ATF at BNL has an acceleration system capable of delivering an electron beam of energies up to 65 MeV, in 0.1 – 2.0 nC bunches with repetition rate of 1.5 Hz. This beam's normalized emittance has been measured to 1 μm at 0.3 nC. As can be seen in Figure 4.1 from right to left, the system has a photoinjector gun, followed by two S-band acceleration cavities, a beam diagnostics and focusing section, and at last the experimental hall with different beam-lines.[1] The photonic gun matches the linac section, that is, the copper-elliptical 1.6 cell is operated in the S-band region (2.586 GHz), at a base pressures of 1×10^{-10} Torr.[39]

In Figure 4.2, we can see more detailed pictures of the different sections of this system. At the top, Figure 4.2 [a], we have the specific section that we are simulating for, and where all the experimental data was taken. The acceleration sections consist of two TW linear acceleration structures from Stanford Linear Accelerator Center (SLAC). The drive power for both cavities comes from a single XK5 klystron tube, also from SLAC. This klystron provides macro-pulses of 3 μs with up to 25 MW, 1 to 6 times per second, and those macro-pulses accelerate electron micro-pulses with repetition rates of up to 81 MHz. The other klystron present in the drawings provides the driving power of the photoinjector electron gun, and it is a SW klystron from Thales. The gun area is magnified in Figure 4.2 [b]. Electrons are extracted from a copper cathode, located in the center of the removable back flange, using a 266 nm laser at around 30 μJ. The QE for this arrangement has been measured to be around 0.01 %. The Thales klystron is connected to the 1.6 elliptical copper cell gun cavity as seen in the image. It can deliver up to 10 MW, although it is typically run at 2.5 MW in 2.5 μs repetition rate, and has a designed accelerating field of 100 MV/m. Following the gun cavity is a 6 coil pack solenoid that compensate for initial thermal

[1] This image is from a previous model that hasn't been updated with the latest modifications to the experimental hall. Currently, the beam-line at the bottom has been removed, and the middle beam-line bending dipole has been redirected towards the lower left corner.

emittance while keeping zero longitudinal magnetic field at the cathode. Through this solenoid runs a 100 A current cooled by water. After the solenoid there is one electron beam monitor right before the accelerator cavities. This monitor is called "LPOP", where L stand for low energy and the POP designation was given in the software used to manipulate these cameras. Lastly, Figure 4.2 [c] at the bottom shows the area right after the beam is accelerated. This section is used for emittance optimization and beam manipulation before it is sent to the experimental area where the users add their probes for experiments. Depict in this image are three "focusing triplets", Q1, Q2 and Q3. Each of these triplets consist of two 10cm long quadruple magnets, with one 20cm long quadrupole in between them. While the data was taken for the analysis presented here, Q1 and Q2 were off, thus creating a long drift space in which emittance could be calculated. In this picture, there are six eBPM named "HPOP's" where the "H" stands for high energy. The bunch compressor shown in the image shortens the beam longitudinal spread to around 100 fs with up to 1 kA peak current.

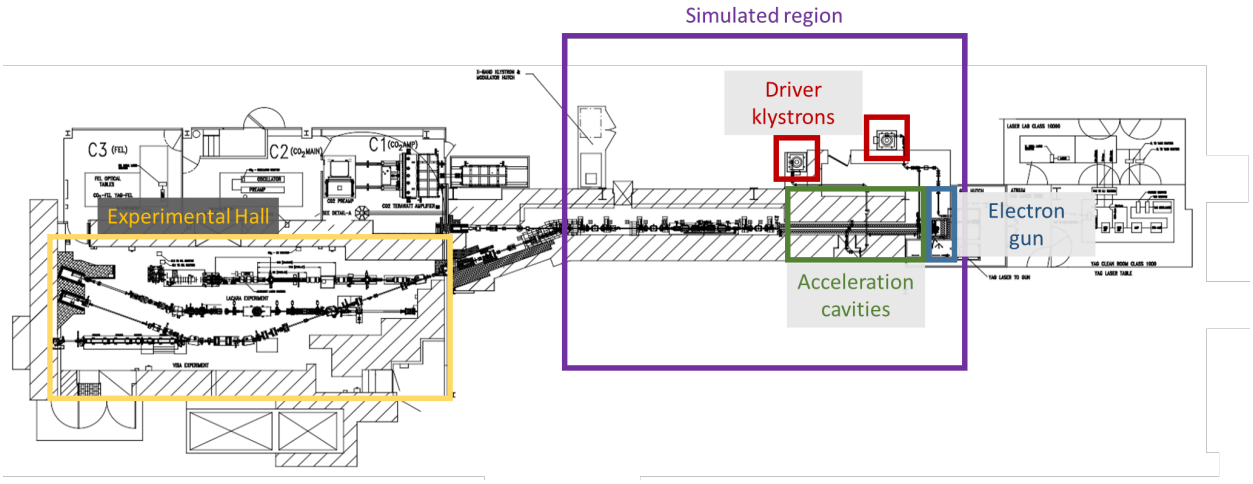

Figure 4.1 Schematic layout of the ATF full system. From right to left, the blue box encapsulates the electron gun, where the electrons are extracted from cathode and focused once, after which follows the acceleration cavities in the green rectangle. These, and the driving klystrons, are all part of the bigger purple rectangle of all the components included in the OPAL simulation. At the lower left corner, the experimental hall is highlighted in a yellow rectangle.

4.1.2 Experimental measurements

Using the Charge-Coupled Device (CCD) cameras at the different locations previously specified of the beamline, we obtained current intensity images for the transverse profile of the electron beam.

These images were then cut to the approximate radius of the beam, in some cases ignoring halo effects and the tale. We determined the edges of the beam by summing over all the rows and columns of each image, and cutting wherever the summed intensity was lower than 55% of the average highest intensity. This method was very successful at determining the radius for the images used for the emittance calculation, but failed to provide an accurate representation of the beam edges for some images taken at HPOP1 when the shape of the beam was particularly dim. For that reason, we modified the code to specifically treat images at HPOP1 with a reduced threshold. Selected images that represent the common trends are presented in Figure 4.3 with their respective trimmed version. The estimated radius for the beam before acceleration ranged from as compressed as 0.52 mm to up to 10 mm, while the range after acceleration was from 0.13 mm (only in one axis while being more prolonged in the other) up to 1.4 mm.

4.1.3 Simulation using OPAL framework

4.1.4 Emittance calculation and comparison

We saw before that the beam emittance is by definition the area enclosed by the beam in space-velocity phase space, mathematically express as in equation 4.1. Here γ, α and β are constants known as the twiss parameters.

$$\epsilon_x = \gamma x^2 + 2\alpha x x' + \beta x'^2 \tag{4.1}$$

According to [40], one can measure the beam emittance using images from the transverse profile of the beam at three different locations where the beam wasn't accelerated, since acceleration can and will change the beam's emittance. Equation 4.2 gives the beam's width based on the measured emittance ϵ, and beta function of the linac $\beta(z)$.

$$w(z) = \sqrt{\beta(z)\epsilon} \tag{4.2}$$

Suppose that we have a electron acceleration system, for which we would like to determine the beam emittance, that follows the diagram in Figure 4.4. To do the calculation at the location of the

dark blue vertical line, we would need three subsequent beam profile monitors at a known distance L_a, L_b and L_c from the reference point,with measured beam width w_a, w_b and w_c respectively. We can use to our advantage the relation 4.3, and solve for two of the twiss parameters and the emittance in the linear equations 4.4.

$$\gamma = \frac{1 + \alpha^2}{\beta} \tag{4.3}$$

$$\begin{aligned} w_a^2 &= \beta\epsilon - 2L_a\alpha\epsilon + L_a^2\gamma\epsilon, \\ w_b^2 &= \beta\epsilon - 2L_b\alpha\epsilon + L_b^2\gamma\epsilon, \\ w_c^2 &= \beta\epsilon - 2L_c\alpha\epsilon + L_c^2\gamma\epsilon \end{aligned} \tag{4.4}$$

Using this approach, we were able to calculate the emittance of the beam at ATF. To find the radius of the beam, we trimmed the images using the sum of the intensities in each column and row for y-axis and x-axis respectively. We evaluated the emittance in both axes, ϵ_x and ϵ_y, as well as for the diagonal, ϵ_{ms}, where the radii for ϵ_{ms} is the diagonal formed between the x and y axes, as described in equation 4.5. We took four consecutive beam profile images from HPOP2, HPOP3, HPOP4 and HPOP5, and made parabolic fittings for the equation 4.1 to obtain the real or geometric emittance. Some results of these fittings are presented in Figure 4.5. We obtained normalized emittance ranging from 0.767 mm-mrad to 5.63 mm-mrad, in agreement with previous measurements.[41]

$$r_{ms} = \sqrt{r_x^2 + r_y^2} \tag{4.5}$$

4.2 Design strategy

4.2.1 Capabilities and specifications of D-line

FRIB is capable of producing ion beams from an assortment of elements, ranging from H to ^{238}U, with energies of over 200 MeV in 0.7 mA current beams of approximately 0.5 mm radius. This beam is produced from the collision of a primary-very-fast stable-isotope beam (generated

using electron-cyclotron resonance sources) with a selected (also stable and usually heavier) target which causes projectile fragmentation, and the resulting unstable isotopes follow particle and energy selection processes.[42] For our interest, we take a closer look at a later portion of the beamline named D-line, where the ion beam's energy is significantly reduced to about 30 keV and can be cooled to a momentum spread as small as $\frac{Deltap}{p} = 10^{-5}$.

4.2.2 Calculations for rare isotope and electron interactions

The number of ions per unit of time, N_τ, that can be confined inside the trap can be estimated from the known parameters of the electron beam charge potential. If we assume that the electron beam is fully neutralized with the ions in the target, such that the total charge for each is the same, we can calculate N_τ as in equation 4.6. In this equation, I_e is the electron current, v is the velocity of the beam, L is the length of the trap , and e is the unit charge of an electron $e = 1.602 \times 10^{-19}$ C.

$$N_\tau = \frac{I_e L}{e v} \tag{4.6}$$

If our electrons have energies of about 150 MeV, they are relativistic and we can calculate their velocity from equation 2.32, and thus estimate the density capacity of the trap. We present such estimates in Table 4.1 for an electron current ranging from 100 mA to 1 A, and assuming 100% efficiency.

Current in A	**# of ions**	**# of electrons**	**Ion density**	**Luminosity in 1/s/cm^2**
0.1	1.04×10^{09}	6.24×10^{17}	5.30×10^{09}	3.31×10^{27}
0.2	2.08×10^{09}	1.25×10^{18}	1.06×10^{10}	1.32×10^{28}
0.3	3.12×10^{09}	1.87×10^{18}	1.59×10^{10}	2.98×10^{28}
0.4	4.16×10^{09}	2.50×10^{18}	2.12×10^{10}	5.29×10^{28}
0.5	5.20×10^{09}	3.12×10^{18}	2.65×10^{10}	8.27×10^{28}
0.6	6.24×10^{09}	3.74×10^{18}	3.18×10^{10}	1.19×10^{29}
0.7	7.28×10^{09}	4.37×10^{18}	3.71×10^{10}	1.62×10^{29}
0.8	8.32×10^{09}	4.99×10^{18}	4.24×10^{10}	2.12×10^{29}
0.9	9.37×10^{09}	5.62×10^{18}	4.77×10^{10}	2.68×10^{29}
1	1.04×10^{10}	6.24×10^{18}	5.30×10^{10}	3.31×10^{29}

Table 4.1 Predicted luminosity and number of ions for a given electron beam current.

According to [43], the electric potential produced by an electron beam can be calculated by the

equation 4.7, with the linear charge density as in equation 4.8. A description of the variables used in these equations, with the assumed values, can be found in Table 4.2, and the resulting potential is presented in Figure 4.6.

$$\phi = \frac{Q_e}{2\pi\epsilon_0} \begin{cases} \left[\frac{1}{2}\left(1 - \frac{r^2}{b^2}\right) + \ln\left(a/b\right)\right], & 0 \leq r \leq b, \\ \ln\left(a/r\right), & b < r \leq a, \end{cases} \tag{4.7}$$

$$Q_e = \frac{-I_e}{\beta c} \leq 0 \tag{4.8}$$

Parameter	**Value**	**Unit**
Electron beam radius b	0.005	m
Beam tube radius a	0.05	m
Permittivity of free space ϵ_0	8.85×10^{-12}	F/m
Electron current I_e	0.5	A
Relativistic electron velocity β	1.00	unit-less
Speed of light c	3.00×10^8	m/s

Table 4.2 Variables used for the calculation of the electric potential produced by an electron beam of 150 MeV.

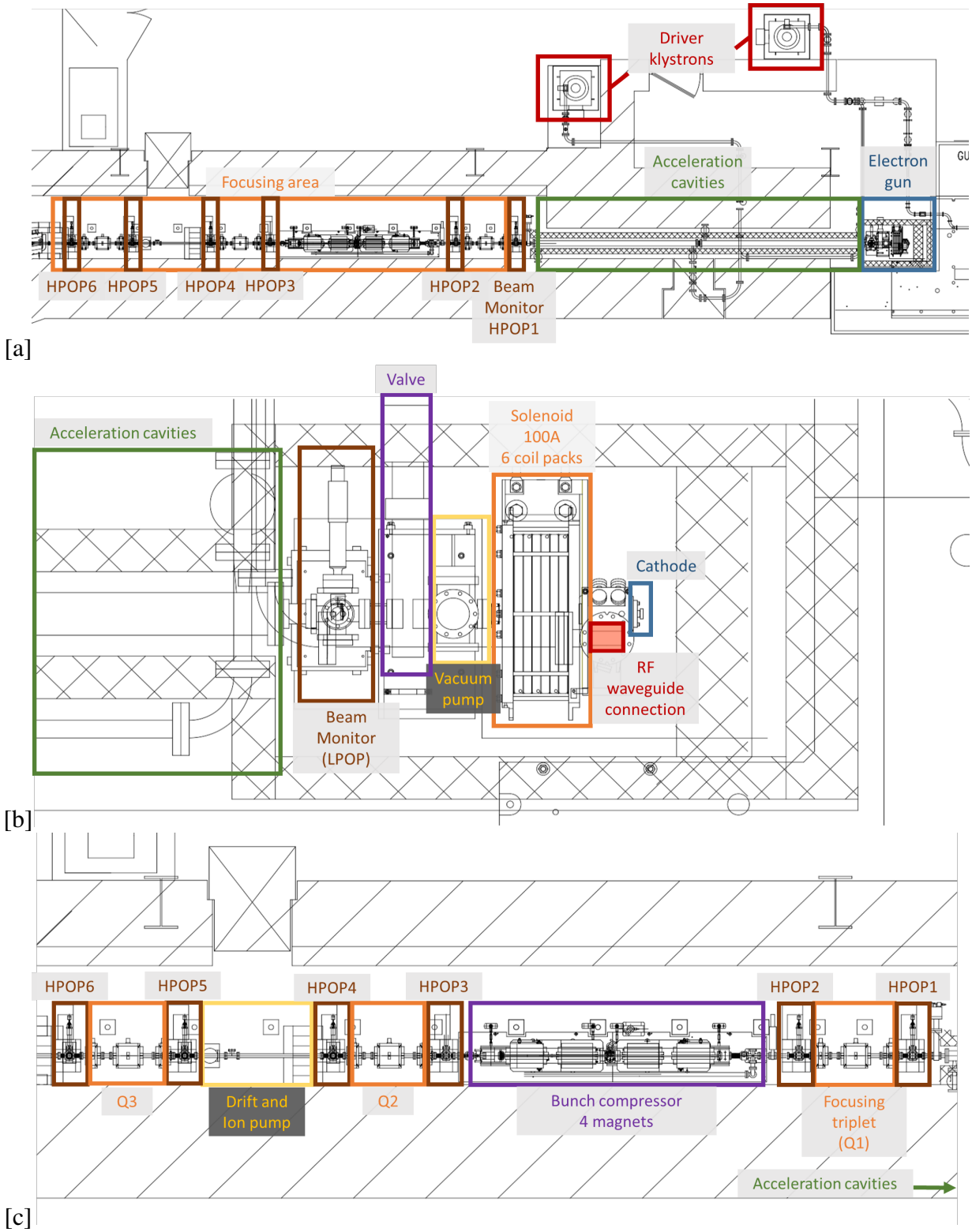

Figure 4.2 Zoomed-in areas of the ATF system. [a] Area simulated using the OPAL software and the locations at which experimental data was collected using eBPM (HPOP's). [b] Components of the electron gun, from extraction up to before acceleration. [c] Systems for beam manipulation and observation after the RF acceleration of the beam.

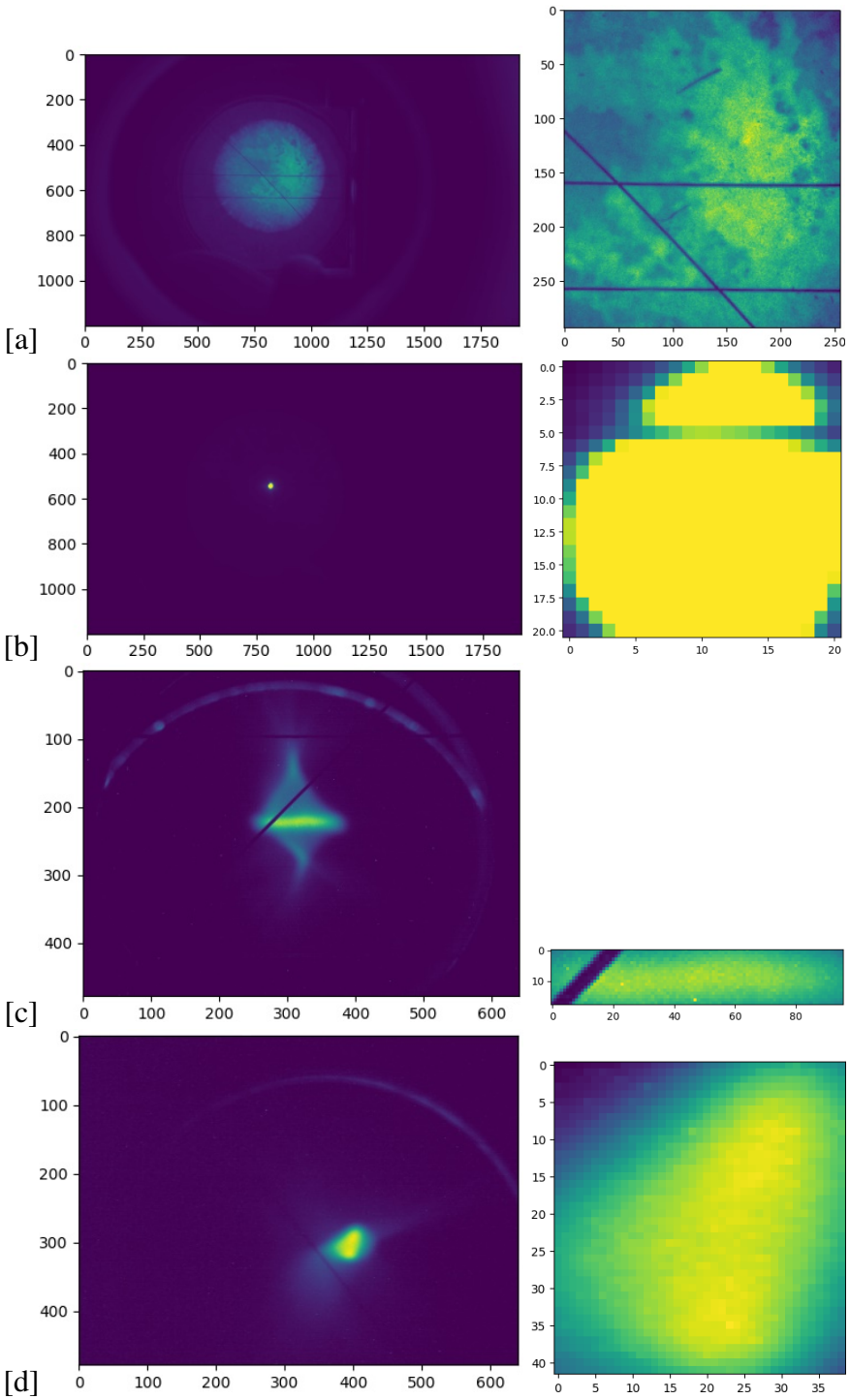

Figure 4.3 Transverse beam profiles of the electron system at ATF unprocessed (left) and after process for beam radii trimming (right), with an RF voltage of 120 V. [a] And [b] were both taken from the first camera, LPOP1. The former was under an RF phase of -9.0°, solenoid current of 105 A and laser power of 30.44 μJ; while the later was under the conditions of -19°, solenoid current of 120 A and laser power of 31.95 μJ. [c] And [d] were taken at locations HPOP2 and HPOP4 respectively, both with RF phase of 31°, solenoid current of 100 A and laser power of 30.72 μJ.

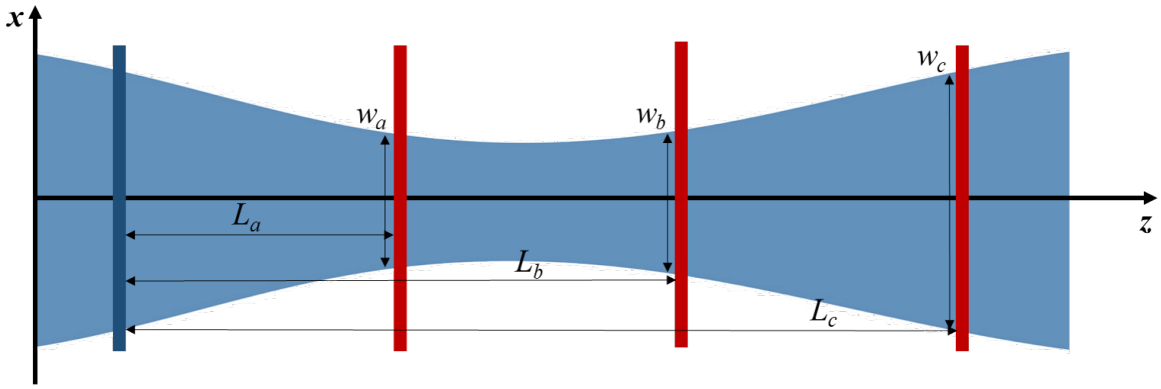

Figure 4.4 Diagram of measurement scheme for emittance in an electron linac. The light blue shade represents the beam's profile, the dark blue vertical line is the reference point where the emittance will be calculated, and the red vertical lines are three positions with beam profile monitors from which we will acquire the data.

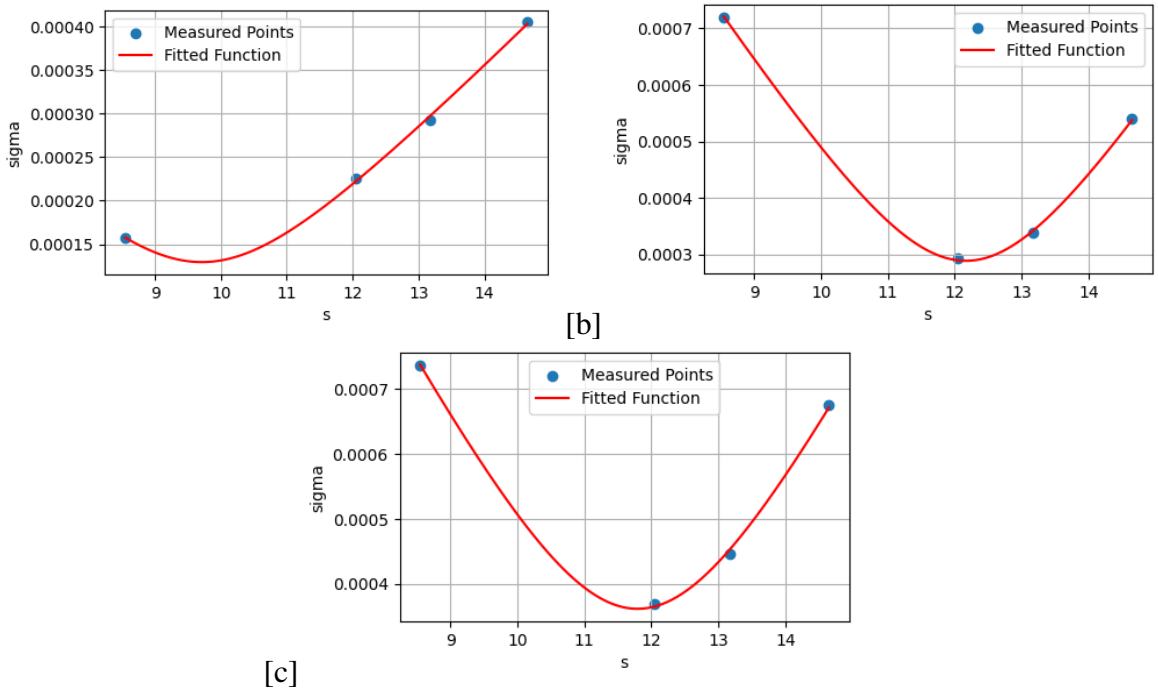

Figure 4.5 Parabolic fittings for measurements of the radii in [a] the x-axis, [b] the y-axis, and [c] the diagonal radius calculated from equation 4.5, for the operational conditions of RF phase of 31°, RF power of 120 V and a solenoid current of 100 A for space charge correction.

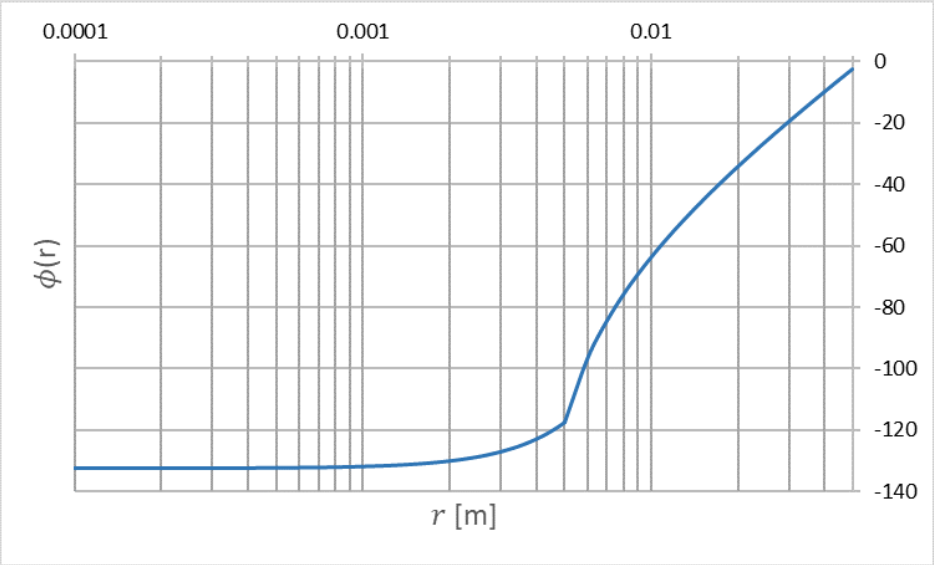

Figure 4.6 Predicted electric potential inside the ion trap.

CHAPTER 5

SAFETY CONSIDERATIONS

5.1 High voltage insulation

In order to maintain a vacuum of $< 1 \times 10^{-9}$ Pa and bear the high temperatures involved in the baking process, Alumina alloys, with concentrations ranging from 92% up to 99.5%, is the most commonly used choice for insulation. We present the properties of different concentrations in Table 5.1. The insulator must be brazed to a metal ring and then either brazed or welded to a vacuum vessel or flange for vacuum preservation. Much consideration must be made to the brazing geometry and material used for joint.

Property	**92%**	**96%**	**99%**	**99.5%**
Compressive Strength [MPa]	2300		2160	2350
Tensile Strength [MPa]	180	193	241	
Young's Modulus	280	320	360	370
Thermal Expansion [40-800 °C, $\times 10^{-6}$ °C^{-1}]	7.8	7.9	8.0	8.0
Thermal Conductivity @ 20 °C [W (m K)$^{-1}$]	18	24	29	32
Dielectric Constant	9.0	9.4	9.9	9.9
RF Loss Factor ($\times 10^{-4}$) @ 1 MHz	54	38	20	10
Volume Resistance @ 20 °C [Ωcm]	$> 10^{14}$	$> 10^{14}$	$> 10^{14}$	$> 10^{14}$
Volume Resistance @ 300 °C [Ωcm]	10^{12}	10^{10}	10^{10}	10^{13}

Table 5.1 Properties of alumina with varying alumina content.[7]

One can do a rough estimate of the needed insulation diameter by using the formula for a coaxial cylinder, equation 5.1, although simulation is needed for the final design.

$$E = \frac{V/R_{inner}}{ln(R_{outer}/R_{inner}} \tag{5.1}$$

where V is the voltage on the central conductor, R_{outer} and R_{inner} are the outer and inner radii for the conductor respectively, and E is the electric field on the inner conductor. The outer conductor is part insulator and part conductor.[7]

CHAPTER 6

DISCUSSION

The Facility for Rare Isotope Beams (FRIB) stands at the forefront in the quest to deepen our understanding of nuclear structure, by providing beams of isotopes with milliseconds lifetimes in the greatest density ever seen. This thesis aimed to investigate the feasibility of integrating an electron beam with FRIB's capabilities to perform electron elastic scattering experiments, thereby contributing to the precise measurement of nuclear charge radii. A comprehensive review of the technology necessary to perform electron elastic scattering off online ions was presented in pair with the theory of the experiment. We discussed the details from the photocathode, explored the option of using thermionic guns, presented the latest advances in compact RF acceleration cavities, explained the technology implemented at RIKEN for the simultaneous trapping and scattering of ions with electrons, and presented information of the science that allows precise measurement of the scattering angle and energy.

The modeling of BNL electron linac helped us understand the structural and operational requirements of an electron beam facility. With the measurement of the transverse beam profile at multiple locations throughout the beamline, we were able to measure the geometrical emittance and from this obtain the normalized emittance. These measurement coincided with those previously observed as well as with the simulation performed using the OPAL open software. The beam radius also agreed, and the effect of the RF phase was observed in the beam profile. This computational model can now be upgraded to RF cavities with higher accelerating gradient, enabling us to see what electron beam can be formed if we build a model with the same technology. These simulations also helped in identifying potential challenges and refining the design parameters to ensure optimal performance.

We also analyzed the electron-ion trapping potential and made an estimate for the achievable luminosity of the system. The ability to trap ions effectively and achieve high luminosity is vital for conducting successful scattering experiments. Our findings indicated that with an electron gun that can provide 100 mA, it is possible to attain a luminosity of up to 3×10^{27} 1/s/cm^2, sufficient

for high-precision measurements of absolute atomic charge radius. High voltage insulation and other safety aspects were considered as well to ensure the safety of the system and the personnel operating it.

The precise measurement of nuclear charge radii for radioactive isotopes will fill a critical gap in our current knowledge, providing essential data for theoretical models. These models are foundational for understanding various nuclear phenomena and for applications in nuclear medicine, astrophysics, and energy research. While this thesis lays the groundwork for integrating an electron acceleration system with FRIB, several avenues for future research and development remain. In the future, the computational model must be expanded to achieve an electron beam with energies above 150 MeV, and potentially the design of the gun should be modified to accommodate for higher currents and subsequently higher brightness. After the electron beam is modelled with the desired parameters, the next step would be build a small prototype of the ion trap, and potentially the electron gun with minimum energy. This will involve collaborative efforts with national labs and engineering teams, followed by rigorous testing to validate the design. Collaborating with researchers from other disciplines, such as materials science and engineering, can bring new perspectives and solutions to the challenges encountered. Interdisciplinary approaches are often key to overcoming complex technical hurdles.

The proposed integration of an electron linac with FRIB represents a bold step towards unlocking new frontiers in nuclear physics. The insights gained from this research will not only enhance our understanding of atomic structures but also pave the way for numerous scientific and technological advancements. This thesis is a testament to the potential of scientific inquiry and the enduring quest for knowledge that drives humanity forward.

BIBLIOGRAPHY

[1] H. De Vries, C.W. De Jager, and C. De Vries. "Nuclear charge-density-distribution parameters from elastic electron scattering". In: *Atomic Data and Nuclear Data Tables* 36.3 (1987), pp. 495–536. ISSN: 0092-640X. DOI: https://doi.org/10.1016/0092-640X(87)90013-1.

[2] I. Angeli and K.P. Marinova. "Table of experimental nuclear ground state charge radii: An update". In: *Atomic Data and Nuclear Data Tables* 99.1 (2013), pp. 69–95. ISSN: 0092-640X. DOI: https://doi.org/10.1016/j.adt.2011.12.006.

[3] B. Povh et al. *Particles and Nuclei: An Introduction to the Physical Concepts*. 7th ed. Graduate Texts in Physics. Springer Berlin, Heidelberg, 2015. ISBN: 978-3-662-46321-5. DOI: 10.1007/978-3-662-46321-5.

[4] K.S. Krane. *Introductory Nuclear Physics*. John Wiley and Sons, 1987. ISBN: 9780471805533.

[5] R. C. Barrett. "Nuclear charge distributions". In: *Reports on Progress in Physics* 37.1 (1974), p. 1. DOI: 10.1088/0034-4885/37/1/001.

[6] Georg Gaertner, Wolfram Knapp, and Richard G. Forbes, eds. *Modern Developments in Vacuum Electron Sources*. 1st ed. Topics in Applied Physics. Springer Cham, 2020. ISBN: 978-3-030-47291-7. DOI: 10.1007/978-3-030-47291-7.

[7] T. Rao and D. H. Dowell. *An Engineering Guide to Photoinjectors*. Independent Publishing Platform, 2014.

[8] K. Wille. *The Physics of Particle Accelerators: An Introduction*. Oxford University Press, 2000. ISBN: 9780198505495.

[9] OpenStax University Physics. *11.5: Particle Accelerators and Detectors - University Physics III - Optics and Modern Physics*. https://phys.libretexts.org/Bookshelves/University_Physics/University_Physics_(OpenStax)/University_Physics_III_-_Optics_and_Modern_Physics_(OpenStax)/11:_Particle_Physics_and_Cosmology/11.05:_Particle_Accelerators_and_Detectors. Accessed on 2024-02-28.

[10] X Cid Vidal and R. Cid Manzano. *Taking a Closer Look at LHC: RF Cavities*. https://www.lhc-closer.es/taking_a_closer_look_at_lhc/0.rf_cavities. Accessed on 2024-02-28.

[11] K M Potter. "Luminosity measurements and calculations; 1985 ed." In: (1985). DOI: 10.5170/CERN-1985-019-V-1.318.

[12] M. Wakasugi. "Electron scattering from unstable nuclei with the SCRIT". in: 2005. URL: https://ribf.riken.jp/RIBF-TAC05/14_SCRIT.pdf. Presentation given at RIBF

TAC05, Japan.

[13] G. Gevorkyan et al. “A cryogenically cooled 200 kV DC photoemission electron gun for ultralow emittance photocathodes”. In: *Review of Scientific Instruments* 94.9 (2023), p. 091501. ISSN: 0034-6748. DOI: 10.1063/5.0160818.

[14] T. Siggins et al. “Performance of a DC GaAs photocathode gun for the Jefferson lab FEL”. in: *Nuclear Instruments and Methods in Physics Research Section A: Accelerators, Spectrometers, Detectors and Associated Equipment* 475.1 (2001). FEL2000: Proc. 22nd Int. Free Electron Laser Conference and 7th F EL Users Workshop, pp. 549–553. ISSN: 0168-9002. DOI: https://doi.org/10.1016/S0168-9002(01)01596-0.

[15] C. Hernandez-Garcia et al. “A High Average Current DC GAAS Photocathode Gun for ERLS and FELS”. in: *Proceedings of the 2005 Particle Accelerator Conference*. 2005, pp. 3117–3119. DOI: 10.1109/PAC.2005.1591383.

[16] D. T. Pierce and F. Meier. “Photoemission of spin-polarized electrons from GaAs”. In: *Phys. Rev. B* 13 (12 1976), pp. 5484–5500. DOI: 10.1103/PhysRevB.13.5484.

[17] Hyeri Lee et al. “A cryogenically cooled high voltage DC photoemission electron source”. In: *Review of Scientific Instruments* 89.8 (2018), p. 083303. ISSN: 0034-6748. DOI: 10.1063/1.5024954.

[18] *Chromacity 520 nm Femtosecond Laser*. Chromacity Lasers. Accessed in 2024. URL: https://chromacitylasers.com/ultrafast-lasers/chromacity-520/.

[19] *PL520B Osram 80 mW 520 nm Green Laser Diode*. Opt Lasers. Accessed in 2024. URL: https://optlasers.com/laser-diodes/pl520b-osram-80-mw-520-nm-laser-diode.

[20] *Spirit-OPA® High Repetition Rate Automated Optical Parametric Amplifier*. Spectra-Physics. Accessed in 2024. URL: https://www.spectra-physics.com/.

[21] B. Dunham, L. Cardman, and C.K. Sinclair. “Emittance Measurements for the Illinois/CEBAF Polarized Electron Source”. In: *Proceedings of 1995 Particle Acceleration Conference* 2 (Apr. 1998). DOI: 10.1109/PAC.1995.505119.

[22] L. Guo et al. “Rugged bialkali photocathodes encapsulated with graphene and thin metal film”. In: *Scientific Reports* 13.1 (2023), pp. 1–12. DOI: 10.1038/s41598-023-29374-6.

[23] J. K. Bae et al. “Operation of Cs–Sb–O activated GaAs in a high voltage DC electron gun at high average current”. In: *AIP Advances* 12.9 (2022), p. 095017. ISSN: 2158-3226. DOI: 10.1063/5.0100794.

[24] K. Pepitone et al. “Operation of a high-current drive beam electron gun prototype for the Compact Linear Collider”. In: *Review of Scientific Instruments* 91.9 (2020), p. 093302.

ISSN: 0034-6748. DOI: 10.1063/5.0013144.

[25] CPI-Eimac. *Model YU-156*. URL: https://www.cpii.com/product.cfm/1/22/131.

[26] P. Sprangle et al. *High Average Current Electron Guns for High-Power FELs*. Naval Research Laboratory. NRL/MR/6790–09-9230. 2009.

[27] W.F. Toonen et al. "Development of a low-emittance high-current continuous electron source". In: *Nuclear Instruments and Methods in Physics Research Section A: Accelerators, Spectrometers, Detectors and Associated Equipment* 1013 (2021), p. 165678. ISSN: 0168-9002. DOI: https://doi.org/10.1016/j.nima.2021.165678.

[28] S. Kutsaev. "Electron bunchers for industrial RF linear accelerators: theory and design guide". In: *European Physical Journal Plus* 136 (Apr. 2021), p. 446. DOI: 10.1140/epjp/s13360-021-01312-3.

[29] E. I. Simakov, V. A. Dolgashev, and S. G. Tantawi. "Advances in high gradient normal conducting accelerator structures". In: *Nuclear Instruments and Methods in Physics Research Section A: Accelerators, Spectrometers, Detectors and Associated Equipment* 907 (2018). Advances in Instrumentation and Experimental Methods (Special Issue in Honour of Kai Siegbahn), pp. 221–230. ISSN: 0168-9002. DOI: https://doi.org/10.1016/j.nima.2018.02.085.

[30] A. D. Cahill et al. "High gradient experiments with X-band cryogenic copper accelerating cavities". In: *Phys. Rev. Accel. Beams* 21 (10 2018), p. 102002. DOI: 10.1103/PhysRevAccelBeams.21.102002.

[31] V. A. Dolgashev et al. "High-gradient rf tests of welded X-band accelerating cavities". In: *Phys. Rev. Accel. Beams* 24 (8 Aug. 2021), p. 081002. DOI: 10.1103/PhysRevAccelBeams.24.081002.

[32] G. E. H. Reuter, E. H. Sondheimer, and Alan Herries Wilson. "The theory of the anomalous skin effect in metals". In: *Proceedings of the Royal Society of London. Series A. Mathematical and Physical Sciences* 195.1042 (1948), pp. 336–364. DOI: 10.1098/rspa.1948.0123.

[33] A. H. McEuen et al. "High-Power Operation of Accelerator Structures at Liquid Nitrogen Temperature". In: *IEEE Transactions on Nuclear Science* 32.5 (1985), pp. 2972–2974. DOI: 10.1109/TNS.1985.4334244.

[34] T. Ohnishi et al. "The SCRIT electron scattering facility project at RIKEN RI beam factory". In: *Physica Scripta* 2015.T166 (2015), p. 014071. DOI: 10.1088/0031-8949/2015/T166/014071.

[35] K. Tsukada et al. "First Observation of Electron Scattering from Online-Produced Radioactive Target". In: *Phys. Rev. Lett.* 131 (9 2023), p. 092502. DOI: 10.1103/PhysRevLett.

131.092502.

[36] T. Ohnishi et al. “The SCRIT electron scattering facility at RIKEN RI Beam Factory”. In: *Nuclear Instruments and Methods in Physics Research Section B: Beam Interactions with Materials and Atoms* 541 (2023), pp. 380–384. ISSN: 0168-583X. DOI: https://doi.org/10.1016/j.nimb.2023.05.038.

[37] Samuel Penner. *Experimental techniques for electron scattering investigations.:* 1970. URL: https://doi.org/10.6028/NBS.TN.523.

[38] F. Sauli. *Gaseous Radiation Detectors: Fundamentals and Applications*. Cambridge University Press, 2014. ISBN: 9781009291200.

[39] Brookhaven National Laboratories: Accelerator Test Facility. *Electron Beam Systems*. https://www.bnl.gov/atf/capabilities/electron-beam-systems.php. Accessed: 2024–03-20.

[40] D. Kayran and M. Fedurin. *Emittance Measurements*. http://case.physics.stonybrook.edu/images/7/73/PHY_542_Emittance_Measurements_2023.pdf. Accessed: 2024–03-12. 2023.

[41] S. G. Biedron et al. “The Operation of the BNL/ATF GUN-IV Photocathode RF Gun at the Advanced Photon Source”. In: (1999). URL: https://cds.cern.ch/record/553651.

[42] G. Machicoane et al. “ARTEMIS-B: A room-temperature test electron cyclotron resonance ion source for the National Superconducting Cyclotron Laboratory at Michigan State University”. In: *Review of Scientific Instruments* 77.3 (Mar. 2006), 03A322. ISSN: 0034-6748. DOI: 10.1063/1.2165749.

[43] S. Schwarz et al. “A high-current electron beam ion trap as a charge breeder for the reacceleration of rare isotopes at the NSCL (invited)”. In: *Review of Scientific Instruments* 79.2 (Feb. 2008), 02A706. ISSN: 0034-6748. DOI: 10.1063/1.2801346.